

NASA Contractor Report CR-187128

Investigation of Advanced Counterrotation Blade Configuration Concepts for High Speed Turboprop Systems

Task IV - Advanced Fan Section Aerodynamic Analysis
Final Report

Andrew J. Crook and Robert A. Delaney
Allison Gas Turbine Division of General Motors
Indianapolis, Indiana

November 1992



Prepared for
Lewis Research Center
Under Contract NAS3-25270

(NASA-CR-187128) INVESTIGATION OF
ADVANCED COUNTERROTATION BLADE
CONFIGURATION CONCEPTS FOR HIGH
SPEED TURBOPROP SYSTEMS. TASK 4:
ADVANCED FAN SECTION AERODYNAMIC
ANALYSIS Final Report, Jul. 1991 -
Jul. 1992 (General Motors Corp.)
74 p

N93-12695

Unclass

G3/07 0129301

481893

Preface

This report was prepared by Andrew J. Crook and Robert A. Delaney of the Allison Gas Turbine Division, General Motors Corporation, Indianapolis, IN. The work was performed under NASA Contract NAS3-25270 from July, 1991 to July, 1992. The modification of the flow analysis for multiple splitter fan/engine geometries was performed by Andrew J. Crook. The Allison program manager for this contract was Robert A. Delaney. The NASA program manager for this contract was Christopher J. Miller.

Acknowledgements

The authors would like to express their appreciation to the following personnel who contributed to this program:

Dr. Edward J. Hall for his suggestions concerning the solver and the many helpful contributions to this document,

Dr. Christopher J. Miller for his review of the program,

UNIX is a trademark of AT&T

IRIS is a trademark of Silicon Graphics, Inc.

TABLE OF CONTENTS

NOTATION	vii
1. SUMMARY	1
2. INTRODUCTION	3
3. EULER/NAVIER-STOKES NUMERICAL ALGORITHM . . .	7
3.1 Nondimensionalization	7
3.2 Governing Equations/Discretization	8
3.3 Fluid Properties	13
3.4 Artificial Dissipation	15
3.5 Time Integration	17
3.6 Implicit Residual Smoothing	18
3.7 Turbulence Model	20
3.8 Boundary Conditions	23
3.9 Solution Procedure	26
4. RESULTS	31
4.1 GMA 3007 Fan Section - Euler Analysis	31
4.2 Energy Efficient Engine Fan Section	41

4.3	Navier Stokes Analysis of Flow Over a Flat Plate	51
4.4	GMA 3007 Fan Section - Navier Stokes Analysis	54
5.	CONCLUSIONS	61
	REFERENCES	63
	APPENDIX A. <i>ADPAC-APES</i> DISTRIBUTION LIST	65

NOTATION

The symbols used in this document and their definitions are listed below for convenience.

Roman Symbols

a ... speed of sound

c_p ... specific heat at constant pressure

c_v ... specific heat at constant volume

e ... internal energy

i ... z index of numerical solution

j ... r index of numerical solution

k ... θ index of numerical solution or thermal conductivity

l ... turbulence model damping function

\vec{n} ... outward unit normal vector

p ... pressure

r ... radius or radial coordinate

t ... time

v ... velocity

z ... axial coordinate

PRECEDING PAGE BLANK NOT FILMED

A ... surface area
 A^+ ... turbulence model parameter
 C_{cp} ... turbulence model parameter
 C_{kleb} ... turbulence model parameter
 C_{wake} ... turbulence model parameter
 CFL ... Courant-Freidrichs-Levy number ($\Delta t / \Delta t_{max, stable}$)
 D ... dissipation flux vector, turbulent damping parameter, or diameter
 F ... flux vector in z direction or turbulence model function
 G ... flux vector in r direction
 H ... flux vector in θ direction
 H_t ... total enthalpy
 K ... source term flux vector or turbulence model parameter
 L ... length
 M ... Mach number
 Pr ... Prandtl number
 $Pr_{turbulent}$... turbulent Prandtl number
 Q ... vector of dependent variables
 R ... gas constant or residual
 S ... blade row correlations or pertaining to surface area normal
 T ... temperature or torque
 V ... volume

Greek Symbols

α ... time-stepping factor

ϵ^2 ... modified second-order damping coefficient
 ϵ^4 ... modified fourth-order damping coefficient
 ρ ... density
 κ^2 ... second-order damping coefficient
 κ^4 ... fourth-order damping coefficient
 γ ... specific heat ratio
 δ ... spatial second-order central difference operator
 λ ... blockage factor
 λ_v ... second coefficient of viscosity ($= -\frac{2}{3}\mu$)
 μ ... coefficient of viscosity
 η ... dimensionless wall normal coordinate ($= y\sqrt{\frac{U_\infty}{\nu x}}$)
 ν ... damping factor
 ω ... angular velocity or vorticity
 Δ ... increment of change

Special Symbols

∇ ... spatial vector gradient operator
 \triangle ... spatial forward difference operator
 ∇ ... spatial backward difference operator

Superscripts

$[\overline{\quad}]$... averaged variable
 $[\sim]$... dimensional variable
 $[\frown]$... implicitly smoothed variable

- $[\vec{\quad}] \dots$ vector variable
- $[\quad]^* \dots$ intermediate variable
- $[\quad]^n \dots$ time step index of variable

Subscripts

- $[\quad]_{effective} \dots$ effective flow value
- $[\quad]_{i,j,k} \dots$ grid point index of variable
- $[\quad]_{inv} \dots$ inviscid component
- $[\quad]_{laminar} \dots$ laminar flow value
- $[\quad]_{max} \dots$ maximum value
- $[\quad]_{min} \dots$ minimum value
- $[\quad]_p \dots$ related to pressure
- $[\quad]_t \dots$ total quantity
- $[\quad]_z \dots$ derivative or value with respect to z
- $[\quad]_r \dots$ derivative or value with respect to r
- $[\quad]_\theta \dots$ derivative or value with respect to θ
- $[\quad]_{turbulent} \dots$ turbulent flow value
- $[\quad]_\infty \dots$ freestream value
- $[\quad]_{ref} \dots$ reference value
- $[\quad]_{kleb} \dots$ Klebanoff intermittency factor
- $[\quad]_{vis} \dots$ viscous component
- $[\quad]_{wake} \dots$ turbulent flow wake parameter
- $[\quad]_2 \dots$ second-order value
- $[\quad]_4 \dots$ fourth-order value

1. SUMMARY

The purpose of this study is the development of a three-dimensional Euler/Navier-Stokes flow analysis for fan section/engine geometries containing multiple blade rows and multiple spanwise flow splitters. An existing procedure developed by Dr J. J. Adamczyk and associates and the NASA Lewis Research Center was modified to accept multiple spanwise splitter geometries and simulate engine core conditions. The procedure was also modified to allow coarse parallelization of the solution algorithm. This document is a final report outlining the development and techniques used in the procedure.

The numerical solution is based upon a finite volume technique with a four stage Runge-Kutta time marching procedure. Numerical dissipation is used to gain solution stability but is reduced in viscous dominated flow regions. Local time stepping and implicit residual smoothing are used to increase the rate of convergence. Multiple blade row solutions are based upon the average-passage system of equations. The numerical solutions are performed on an H-type grid system, with meshes being generated by the system (TIGG3D) developed earlier under this contract. The grid generation scheme meets the average-passage requirement of maintaining a common axisymmetric mesh for each blade row grid.

The analysis was run on several geometry configurations ranging from one to five blade rows and from one to four radial flow splitters. Pure internal flow solutions were obtained as well as solutions with flow about the cowl/nacelle and various engine core flow conditions. The efficiency of the solution procedure was shown to be the same as the original analysis.

2. INTRODUCTION

This document contains the Final Report for the *ADPAC-APES* (Advanced Ducted Propfan Analysis Codes-Average Passage Engine Simulation) program developed by the Allison Gas Turbine Division of the General Motors Corporation under Task IV of NASA Contract NAS3-25270. The objective of this task is development of a three-dimensional flow analysis tool for advanced fan section and turbofan engine geometries such as the NASA/GE Energy Efficient Engine seen in Fig. 2.1 . The tool is able to compute steady flow solutions about geometries with any number of blade rows and axisymmetric radial flow splitters. The tool computes the flow through the fan and optionally about the fan cowl and engine nacelle, both upstream and downstream of the engine. When the domain is extended in this manner, engine performance can be determined entirely by the analysis tool. Effects of engine core flow can also be simulated.

Details of the flow solution algorithm are covered in Chapter three of this document. Chapter four presents solution results for various geometries and comparisons to experimental data. A summary of the conclusions for this study is given in chapter five.

This flow analysis tool was developed from a code entitled *VSTAGE* which was developed by John J. Adamczyk of the NASA Lewis Research Center [1] . The user is

referred to the documentation for that code for additional information on the solution procedure.

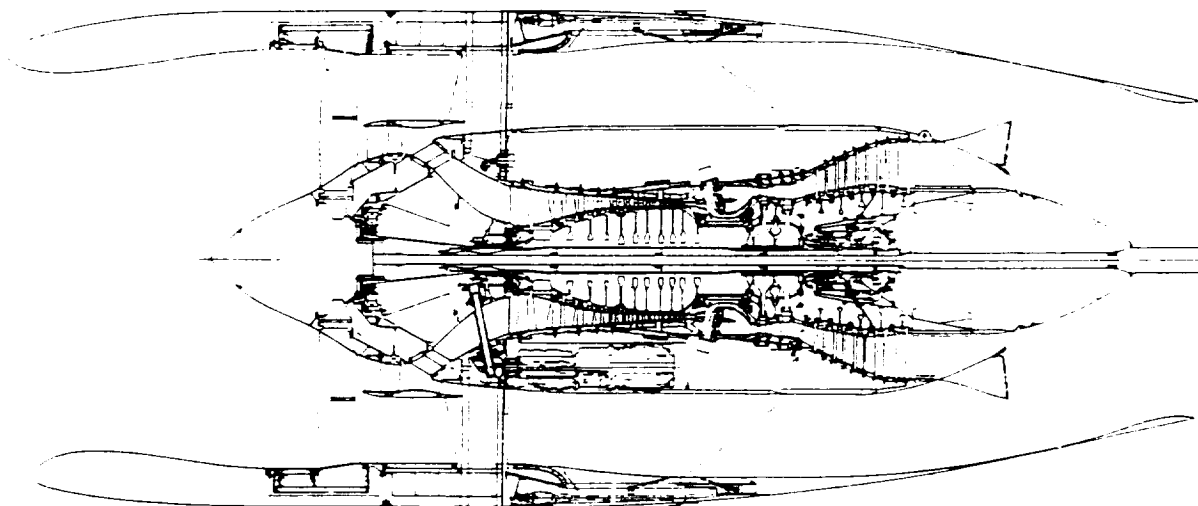


Figure 2.1: NASA/GE Energy Efficient Engine cross section

3. EULER/NAVIER-STOKES NUMERICAL ALGORITHM

This chapter describes the algorithm for the flow solver and outlines a solution procedure for multiple blade row calculations. As stated earlier, the solver was primarily developed by J. J. Adamczyk [1] [2] which was based upon a procedure originated by Jameson [3]. The definitions of the pertinent variables used in this chapter may be found in the Nomenclature.

3.1 Nondimensionalization

The variables in the numerical solution are nondimensionalized by reference values as follows:

$$\begin{aligned} z &= \frac{\tilde{z}}{L_{ref}}, & r &= \frac{\tilde{r}}{L_{ref}}, & v_z &= \frac{\tilde{v}_z}{v_{ref}}, & v_r &= \frac{\tilde{v}_r}{v_{ref}}, & v_\theta &= \frac{\tilde{v}_\theta}{v_{ref}} \\ p &= \frac{\tilde{p}}{p_{ref}}, & \mu &= \frac{\tilde{\mu}}{\mu_{ref}}, & c_p &= \frac{\tilde{c}_p}{R_{ref}}, & c_v &= \frac{\tilde{c}_v}{R_{ref}}, & k &= \frac{\tilde{k}}{k_{ref}} \\ T &= \frac{\tilde{T}}{T_{ref}}, & \rho &= \frac{\tilde{\rho}}{\rho_{ref}}, & \omega &= \frac{\tilde{\omega} L_{ref}}{v_{ref}} \end{aligned} \quad (3.1)$$

The reference quantities are defined as follows:

L_{ref} The maximum diameter of the blade represented in the grid

p_{ref} The reference (or freestream) relative total pressure

ρ_{ref}	The reference (or freestream) relative total density
v_{ref}	The reference (or freestream) velocity determined from the relative total conditions $v_{ref} = \sqrt{p_{ref}/\rho_{ref}}$
μ_{ref}	The reference (or freestream) viscosity
k_{ref}	The reference (or freestream) thermal conductivity
R_{ref}	The reference (or freestream) gas constant
T_{ref}	The reference (or freestream) temperature

3.2 Governing Equations/Discretization

The numerical solution procedure is based on the strong conservation law form of the Navier-Stokes equations expressed in a cylindrical coordinate system. The Euler equations may be derived as a subset of the Navier-Stokes equations by neglecting viscous dissipation and thermal conductivity terms (i.e. - μ and $k = 0$). A derivation of the average-passage equation system can be found in [4]. For a multi-blade row environment, this equation system is obtained by filtering the Navier-Stokes equations in time and space to remove all information except the time average flowfield pertaining to a specific blade row. For the particular blade row, integration of these equations over a rotating finite control volume produces the following equations:

$$\int \frac{\partial}{\partial t}(\lambda Q) dV + L_{inv}(\lambda Q) = \int \lambda S dV + \int \lambda K dV + L_{vis}(\lambda Q) \quad (3.2)$$

The vector of dependent variables Q is defined as:

$$Q = \begin{bmatrix} \rho \\ \rho v_z \\ \rho v_r \\ \rho v_\theta \\ \rho e_t \end{bmatrix} \quad (3.3)$$

where the velocity components v_z, v_r , and v_θ are the absolute velocity components in the axial, radial, and circumferential directions of the coordinate system for the fan section (see Fig. 3.1), respectively. The term λ represents the neighboring blade row blockage factor. This factor has a value between zero and one, with a value of one indicating zero thickness for neighboring blades.

The term λS contains the body forces, energy sources, and momenta correlations associated with the neighboring blade rows. The terms L_{inv} and L_{vis} represent the cell face mass, momentum, and energy flux evaluations for the inviscid, and viscous components, respectively. These terms are defined as:

$$L_{inv}(\lambda Q) = \int_{dA} \left[\lambda \bar{F}_{inv} dA_z + \lambda \bar{G}_{inv} dA_r + \lambda (\bar{H}_{inv} - r\omega \bar{Q}) dA_\theta \right] \quad (3.4)$$

and:

$$L_{vis}(\lambda Q) = \int_{dA} \left[\lambda \bar{F}_{vis} dA_z + \lambda \bar{G}_{vis} dA_r + \lambda (\bar{H}_{vis} - r\omega \bar{Q}) dA_\theta \right] \quad (3.5)$$

The individual flux functions are defined as:

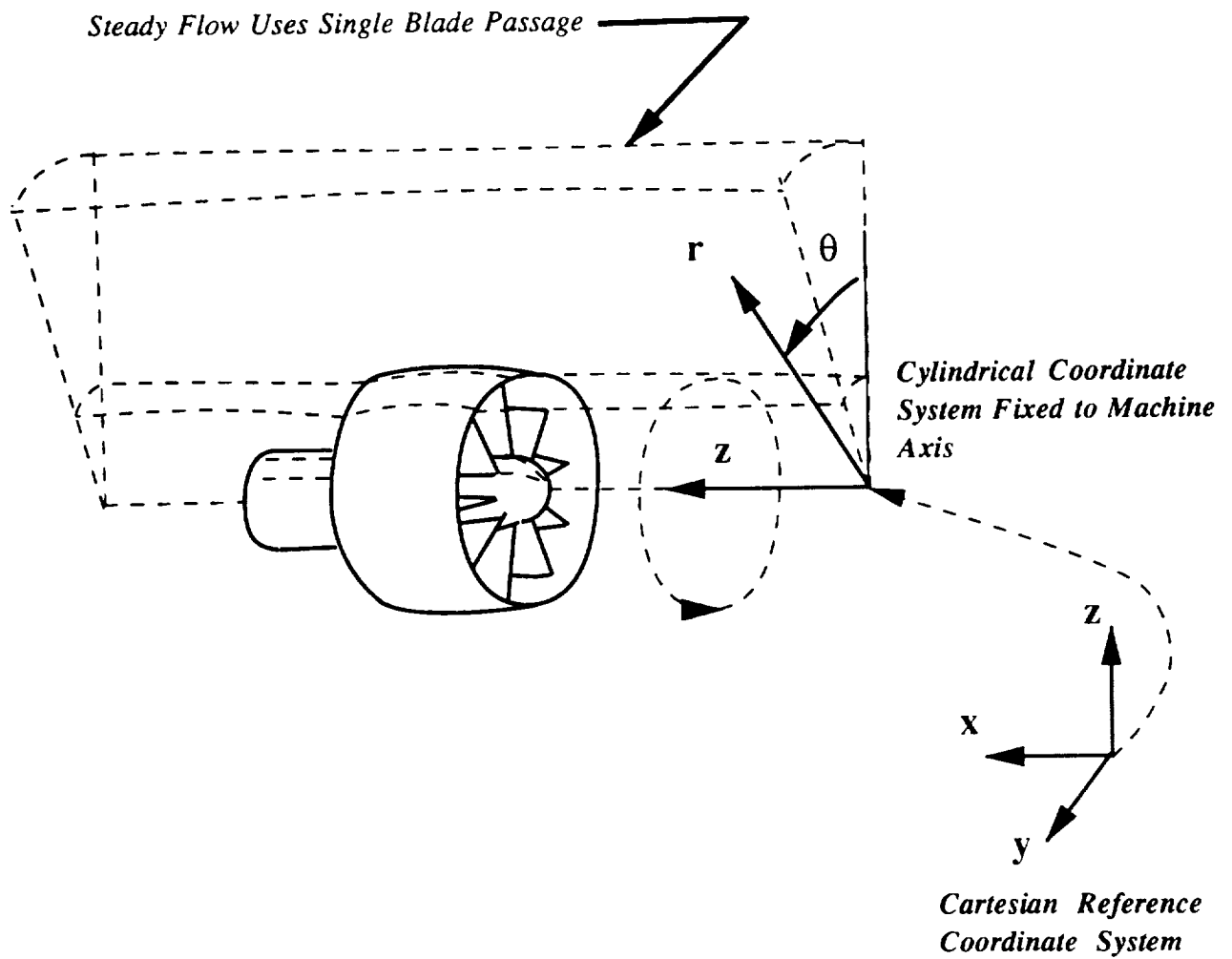


Figure 3.1: Fan section/engine analysis computational domain

$$F_{inv} = \begin{bmatrix} \rho v_z \\ \rho v_z^2 + p \\ \rho v_z v_r \\ r \rho v_z v_\theta \\ \rho v_z H \end{bmatrix}, \quad G_{inv} = \begin{bmatrix} \rho v_r \\ \rho v_z v_r \\ \rho v_r^2 + p \\ r \rho v_r v_\theta \\ \rho v_r H \end{bmatrix}, \quad H_{inv} = \begin{bmatrix} \rho v_\theta \\ \rho v_z v_\theta \\ \rho v_r v_\theta \\ r(\rho v_\theta^2 + p) \\ \rho v_\theta H \end{bmatrix} \quad (3.6)$$

$$F_{vis} = \begin{bmatrix} 0 \\ \tau_{zz} \\ \tau_{zr} \\ \tau_{z\theta} \\ q_z \end{bmatrix}, \quad G_{vis} = \begin{bmatrix} 0 \\ \tau_{rz} \\ \tau_{rr} \\ \tau_{r\theta} \\ q_r \end{bmatrix}, \quad H_{vis} = \begin{bmatrix} 0 \\ \tau_{\theta z} \\ \tau_{\theta r} \\ \tau_{\theta\theta} \\ q_\theta \end{bmatrix}, \quad (3.7)$$

$$\bar{F} = F(\bar{Q}), \quad \bar{G} = G(\bar{Q}), \quad \bar{H} = H(\bar{Q})$$

$$\bar{F}_v = F_v(\bar{Q}), \quad \bar{G}_v = G_v(\bar{Q}), \quad \bar{H}_v = H_v(\bar{Q}) \quad (3.8)$$

The flux variables \bar{F} , \bar{G} , and \bar{H} are determined at each grid cell interface by determining the average (\bar{Q}) of the cell-centered dependent variables from the individual finite volumes adjoining the interface.

Finally, the cylindrical coordinate system source term is:

$$K = \begin{bmatrix} 0 \\ 0 \\ \frac{\rho v_\theta^2 + p}{r} - \tau_{\theta\theta} \\ 0 \\ 0 \end{bmatrix} \quad (3.9)$$

It should be noted that in the numerical algorithm, the radius used in the cylindrical source term K is carefully formulated to guarantee numerical conservation for the

radial momentum equation. That is, for a uniform stagnant flow, the radius in the radial momentum equation is chosen such that both sides of the radial momentum equation are equal. This ensures that small geometric errors do not corrupt the conservative nature of the numerical scheme.

The total energy function, e_t , is defined as:

$$e_t = \frac{p}{(\gamma - 1)\rho} + \frac{1}{2}(v_z^2 + v_r^2 + v_\theta^2) \quad (3.10)$$

The total enthalpy, H , is related to the total energy by:

$$H = e_t + \frac{p}{\rho} \quad (3.11)$$

The viscous stress terms may be expressed as:

$$\tau_{zz} = 2\mu \left(\frac{\partial v_z}{\partial z} \right) + \lambda_v \nabla \cdot \vec{V}, \quad (3.12)$$

$$\tau_{zr} = \mu \left[\left(\frac{\partial v_r}{\partial z} \right) + \left(\frac{\partial v_z}{\partial r} \right) \right], \quad (3.13)$$

$$\tau_{z\theta} = 2\mu \left[\left(\frac{1}{r} \frac{\partial v_r}{\partial \theta} \right) + \left(\frac{\partial v_\theta}{\partial z} \right) \right], \quad (3.14)$$

$$\tau_{rr} = 2\mu \left(\frac{\partial v_r}{\partial r} \right) + \lambda_v \nabla \cdot \vec{V}, \quad (3.15)$$

$$\tau_{r\theta} = 2\mu \left[\left(\frac{1}{r} \frac{\partial v_r}{\partial \theta} \right) + \left(\frac{\partial v_\theta}{\partial r} \right) - \left(\frac{v_\theta}{r} \right) \right], \quad (3.16)$$

$$\tau_{\theta\theta} = 2\mu \left(\frac{1}{r} \frac{\partial v_\theta}{\partial \theta} + \frac{\partial v_r}{r} \right) + \lambda_v \nabla \cdot \vec{V}, \quad (3.17)$$

$$q_z = v_z \tau_{zz} + v_r \tau_{zr} + v_\theta \tau_{z\theta} + k \frac{\partial T}{\partial z}, \quad (3.18)$$

$$q_r = v_z \tau_{rz} + v_r \tau_{rr} + v_\theta \tau_{r\theta} + k \frac{\partial T}{\partial r}, \quad (3.19)$$

$$q_\theta = v_z \tau_{\theta z} + v_r \tau_{\theta r} + v_\theta \tau_{\theta \theta} + k \frac{\partial T}{\partial \theta}, \quad (3.20)$$

where μ is the first coefficient of viscosity, λ_v is the second coefficient of viscosity, and:

$$\nabla \cdot \vec{V} = \frac{\partial u_z}{\partial z} + \frac{\partial u_r}{\partial r} + \frac{1}{r} \frac{\partial u_\theta}{\partial \theta} + \frac{u_r}{r} \quad (3.21)$$

The remaining viscous stress terms are defined through the identities:

$$\tau_{rz} = \tau_{zr}, \quad (3.22)$$

$$\tau_{\theta r} = \tau_{r\theta}, \quad (3.23)$$

$$\tau_{\theta z} = \tau_{z\theta}, \quad (3.24)$$

This integral form of the governing equations is applied to a generalized finite volume in physical space as shown in Fig. 3.2. The cell surface areas dA_z , dA_r , and dA_θ are calculated using the cross product of the diagonals of a cell face, and the cell volume is determined by a procedure outlined by Hung and Kordulla [5] for generalized nonorthogonal cells.

3.3 Fluid Properties

The fluid is assumed to be air acting as a perfect gas, thus the ideal gas equation of state has been used. Fluid properties such as specific heats, specific heat ratio, and Prandtl number are assumed to be constant. The fluid viscosity is derived from the Sutherland formula:

$$\mu = C_1 \frac{(T)^{\frac{3}{2}}}{T + C_2} \quad (3.25)$$

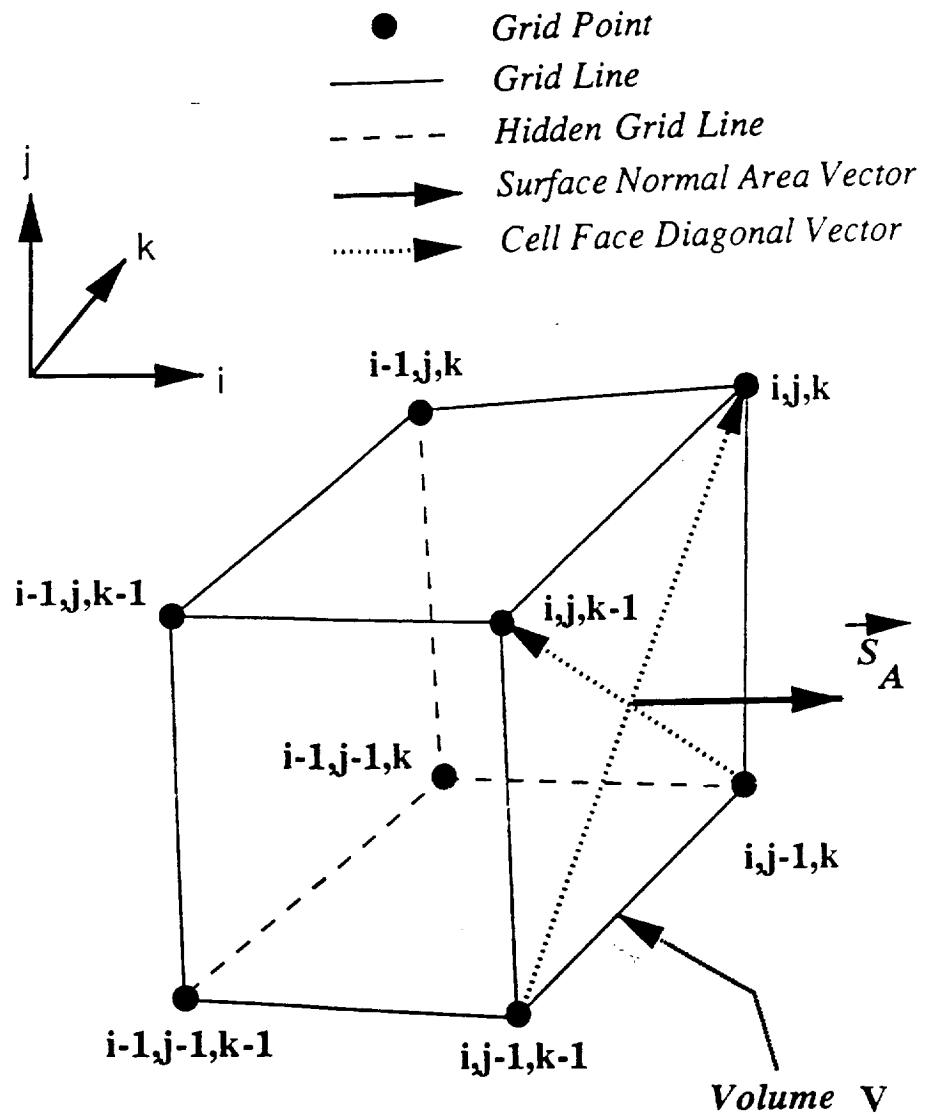


Figure 3.2: Three-dimensional finite volume cell

The so-called second coefficient of viscosity λ_v is fixed according to:

$$\lambda_v = -\frac{2}{3}\mu \quad (3.26)$$

The thermal conductivity is determined from the viscosity and the definition of the Prandtl number as:

$$k = \frac{cp\mu}{Pr} \quad (3.27)$$

3.4 Artificial Dissipation

The discretized system of equations has unstable properties and can exhibit odd-even point decoupling, especially near regions where high gradients of the flow quantities Q exist (e.g., shocks). To suppress these instabilities, an artificial dissipation operator (D) is added to the numerical scheme. Jameson [3] demonstrated that a dissipative system combining second- and fourth-difference smoothing terms can effectively eliminate undesirable numerical oscillations without destroying the accuracy of the solution.

The dissipation operator for the first index is shown below:

$$Dz(Q) = d_{i+\frac{1}{2},j,k} - d_{i-\frac{1}{2},j,k} \quad (3.28)$$

$$d_{i+\frac{1}{2},j,k} = \frac{V_{i+\frac{1}{2},j,k}}{(\Delta t_i)_{i+\frac{1}{2},j,k}} \left[(\epsilon_2)_{i+\frac{1}{2},j,k} \Delta_z Q_{i+\frac{1}{2},j,k} - (\epsilon_4)_{i+\frac{1}{2},j,k} \Delta_z^3 Q_{i+\frac{1}{2},j,k} \right] \quad (3.29)$$

where:

$$(\epsilon_2)_{i+\frac{1}{2},j,k} = \kappa^2 \max(\nu_{i+1,j,k}, \nu_{i,j,k}) \quad (3.30)$$

$$(\epsilon_4)_{i+\frac{1}{2},j,k} = \max(0, \kappa^4 - \epsilon_{i+\frac{1}{2},j,k}^2) \quad (3.31)$$

$$\nu_{i,j,k} = \frac{|p_{i+1,j,k} - 2p_{i,j,k} + p_{i-1,j,k}|}{|p_{i+1,j,k} + 2p_{i,j,k} + p_{i-1,j,k}|} \quad (3.32)$$

Typical values for the second and fourth difference damping constants are:

$$\kappa^2 = \frac{1}{4} \quad \kappa^4 = \frac{1}{64} \quad (3.33)$$

The term Δt_i represents a one-dimensional equivalent of the maximum allowable time step in the given coordinate direction. The use of this factor introduces an eigenvalue scaling into the dissipation operator which minimizes the added dissipation in coordinate directions which do not limit the stability of the algorithm.

The scheme presented above is stable for all time steps satisfying the *CFL*-related time step limitation

$$CFL \leq 2\sqrt{2} \quad (3.34)$$

The damping scheme described above may be applied directly for inviscid flow calculations, but must be modified slightly for viscous flow calculations. In regions of the flowfield where viscous dissipation increases, the artificial dissipation should be reduced. In order to produce this effect, a Mach number scaling is employed and the modified second and fourth difference coefficients are shown below.

$$(\epsilon_2)_{i+\frac{1}{2},j,k} = \kappa^2 \max(\nu_{i+1,j,k}, \nu_{i,j,k}) \min\left(\frac{M_{i+\frac{1}{2},j,k}}{\bar{M}}, 1\right) \quad (3.35)$$

$$(\epsilon_4)_{i+\frac{1}{2},j,k} = \max(0, (\kappa^4) \min\left(\frac{M_{i+\frac{1}{2},j,k}}{\bar{M}}, 1\right) - (\epsilon_2)_{i+\frac{1}{2},j,k}) \quad (3.36)$$

where \bar{M} is the mid passage or free stream Mach number.

The complete dissipation operator $D_{i,j,k}$ is constructed as the sum of the dissipation operators in each of the respective coordinate directions as:

$$D_{i,j,k} = (D_z)_{i,j,k} + (D_r)_{i,j,k} + (D_\theta)_{i,j,k} \quad (3.37)$$

3.5 Time Integration

The time-stepping scheme used to advance the discretized equations is a four-stage Runge-Kutta integration. The solution proceeds as:

$$\begin{aligned} Q_1 &= Q^n - \alpha_1 \Delta t [L(Q^n) + D(Q^n)], \\ Q_2 &= Q^n - \alpha_2 \Delta t [L(Q_1) + D(Q^n)], \\ Q_3 &= Q^n - \alpha_3 \Delta t [L(Q_2) + D(Q^n)], \\ Q_4 &= Q^n - \alpha_4 \Delta t [L(Q_3) + D(Q^n)], \\ Q^{n+1} &= Q_4 \end{aligned} \quad (3.38)$$

where:

$$\alpha_1 = \frac{1}{8}, \quad \alpha_2 = \frac{1}{4}, \quad \alpha_3 = \frac{1}{2}, \quad \alpha_4 = 1 \quad (3.39)$$

and:

$$L(Q) = L_{inv}(Q) - L_{vis}(Q) \quad (3.40)$$

Linear stability analysis indicates that this scheme is stable for all time increments Δt which satisfy the stability criteria $CFL \leq 2\sqrt{2}$. The CFL number may be defined in a one-dimensional manner as:

$$CFL = \frac{\Delta t}{\frac{|u|+a}{\Delta z}} \quad (3.41)$$

This factor is calculated for each coordinate direction, and then geometrically averaged to obtain the maximum allowable time increment for a given computational cell.

The acceleration technique known as local time stepping is used to enhance convergence to the steady-state solution. Local time stepping utilizes the maximum allowable time increment at each finite volume cell during the course of the solution. If a truly unsteady flow calculation is desired, a uniform value of the time step Δt must be used at every cell to maintain the time-accuracy of the solution.

3.6 Implicit Residual Smoothing

Implicit residual smoothing is used to extend the stability limit of the algorithm and increase the rate of convergence to a steady state solution. Residual smoothing attempts to accelerate the propagation of changes in the dependent variables by filtering the residuals of the calculation (which may also be interpreted as the local time derivative of the computational solution) at each time step. By enhancing the transfer of information between grid points, calculation time steps much larger than the stability-limited values may be utilized. Residual smoothing was originally introduced by Lerat (see e.g. Hollanders, et al. [6]) for use with the Lax-Wendroff scheme and later applied to Runge-Kutta schemes by Jameson and Baker [7] as a technique to accelerate convergence for steady-state calculations.

Since the time rate of change of the dependent variables $\partial Q / \partial t$ is in essence controlled by a residual operator $R(Q) = L(Q) - D(Q)$, it would follow that any measure which accelerates the propagation of changes in the residual throughout

the domain would ultimately enhance convergence. The implicit residual smoothing operator used in this study can be written as:

$$(1 - \epsilon_z \delta_{zz})(1 - \epsilon_r \delta_{rr})(1 - \epsilon_\theta \delta_{\theta\theta}) \hat{R}_{i,j,k} = R_{i,j,k} \quad (3.42)$$

where the differencing operator δ is expressed as:

$$\delta_{zz} R_{i,j,k} = R_{i+1,j,k} - 2R_{i,j,k} + R_{i-1,j,k} \quad (3.43)$$

A value of $\epsilon_{zz} = \epsilon_{rr} = \epsilon_{\theta\theta} = 2$ is typically used.

The reduction is applied along each coordinate direction separately as:

$$R_{i,j,k}^* = (1 - \epsilon_z \delta_{zz})^{-1} R_{i,j,k} \quad (3.44)$$

$$R_{i,j,k}^{**} = (1 - \epsilon_r \delta_{rr})^{-1} R_{i,j,k}^* \quad (3.45)$$

$$R_{i,j,k}^{***} = (1 - \epsilon_\theta \delta_{\theta\theta})^{-1} R_{i,j,k}^{**} \quad (3.46)$$

$$\hat{R}_{i,j,k} = R_{i,j,k}^{***} \quad (3.47)$$

where each of the first three steps above requires the inversion of a scalar tridiagonal matrix. The residual smoothing operator is applied to the first and third stage of the four-stage Runge-Kutta algorithm. The time-marching scheme then becomes:

$$\begin{aligned} Q_1 &= Q^n - \alpha_1 \hat{R}(Q^n) \\ Q_2 &= Q^n - \alpha_2 R(Q_1) \\ Q_3 &= Q^n - \alpha_3 \hat{R}(Q_2) \\ Q_4 &= Q^n - \alpha_4 R(Q_3) \\ Q^{n+1} &= Q_4 \end{aligned} \quad (3.48)$$

The implicit residual smoothing operator applied in this context allows a time step greater than the unsmoothed stability limited step. For example, the new time step limit for the axial coordinate must satisfy:

$$\epsilon_z \geq \frac{1}{4} \left[\left(\frac{CFL_{smooth}}{CFL} \right)^2 - 1 \right] \quad (3.49)$$

Thus with the unsmoothed stability criteria ($CFL \leq 2\sqrt{2}$), a sample of new limits is listed below.

$$\epsilon_z = 1.0 \quad CFL_{smooth} \leq 6.32$$

$$\epsilon_z = 2.0 \quad CFL_{smooth} \leq 8.48$$

$$\epsilon_z = 3.0 \quad CFL_{smooth} \leq 10.19$$

3.7 Turbulence Model

The effects of turbulence are accounted for with a relatively standard version of the Baldwin-Lomax [8] turbulence model. This model is computationally efficient, and has been successfully applied to a wide range of geometries and flow conditions.

The effects of turbulence are introduced into the numerical scheme by utilizing the Boussinesq approximation, resulting in an effective calculation viscosity defined as:

$$\mu_{effective} = \mu_{laminar} + \mu_{turbulent} \quad (3.50)$$

The simulation is therefore performed using an effective viscosity which combines the effects of the physical (laminar) viscosity and the effects of turbulence through the turbulence model and the turbulent viscosity $\mu_{turbulent}$.

The Baldwin-Lomax model specifies that the turbulent viscosity be based on an inner and outer layer of the boundary layer flow region as:

$$\mu_{turbulent} = \begin{cases} (\mu_{turbulent})_{inner}, & y \leq y_{crossover} \\ (\mu_{turbulent})_{outer}, & y > y_{crossover} \end{cases} \quad (3.51)$$

where y is the normal distance to the nearest wall, and $y_{crossover}$ is the smallest value of y at which values from the inner and outer models are equal. The inner and outer model turbulent viscosities are defined as:

$$(\mu_{turb})_{inner} = \rho l^2 |\omega| \quad (3.52)$$

$$(\mu_{turb})_{outer} = K C_{cp} \rho F_{wake} F_{kleb} y \quad (3.53)$$

Here, the term l is the Van Driest damping factor

$$l = ky(1 - e^{(-y^+/A^+)}) \quad (3.54)$$

ω is the vorticity magnitude, F_{wake} is defined as:

$$F_{wake} = y_{max} F_{max} \quad (3.55)$$

where the quantities y_{max} , F_{max} are determined from the function

$$F(y) = y|\omega|[1 - e^{(-y^+/A^+)})] \quad (3.56)$$

The term y^+ is defined as

$$y^+ = y \sqrt{\frac{\rho|\omega|}{\mu_{laminar}}} \quad (3.57)$$

The quantity F_{max} is the maximum value of $F(y)$ that occurs in a profile, and y_{max} is the value of y at which it occurs. The determination of F_{max} and y_{max} is perhaps the most difficult aspect of this model for three-dimensional flows. The profile of $F(y)$

versus y can have several local maximums, and it is often difficult to establish which values should be used. It has been found from numerical experimentation that the most reliable value of F_{max} is taken as the maximum value of $F(y)$ between a y^+ value of 350.0 and 1200.0. The function F_{kleb} is the Klebanoff intermittency factor given by

$$F_{kleb}(y) = [1 + 5.5(\frac{C_{kleb}y}{y_{max}})^6]^{-1} \quad (3.58)$$

and the remainder of the terms are constants defined as:

$$A^+ = 26,$$

$$C_{cp} = 1.6,$$

$$C_{kleb} = 0.3,$$

$$k = 0.4,$$

$$K = 0.0168 \quad (3.59)$$

In practice, the turbulent viscosity is limited such that it never exceeds 1000.0 times the laminar viscosity.

The turbulent flow thermal conductivity term is also treated as the combination of a laminar and turbulent quantity as:

$$k_{effective} = k_{laminar} + k_{turbulent} \quad (3.60)$$

For turbulent flows, the turbulent thermal conductivity $k_{turbulent}$ is determined from a turbulent Prandtl number $Pr_{turbulent}$ such that

$$Pr_{turbulent} = \frac{c_p \mu_{turbulent}}{k_{turbulent}} \quad (3.61)$$

The turbulent Prandtl number is normally chosen to have a value of 0.9.

In order to properly utilize this turbulence model, a fairly large number of grid cells must be present in the boundary layer flow region, and, perhaps of greater importance, the spacing of the first grid cell off of a wall should be small enough to accurately account for the inner “law of the wall” turbulent boundary layer profile region. This requires the first cell in the laminar sublayer with a y^+ value typically around 5. Unfortunately, this constraint is typically not satisfied due to grid-induced problems or excessive computational costs, especially for multiple blade row calculations. Practical applications of the Baldwin-Lomax model for three-dimensional viscous flow must be made with the limitations of the model in mind. The Baldwin-Lomax model was designed for the prediction of wall bounded turbulent shear layers, and is not likely to be well suited for flows with massive separations or large vortical structures.

3.8 Boundary Conditions

Inflow and exit boundary conditions are applied numerically using characteristic theory. A one-dimensional isentropic system of equations is utilized to derive the following characteristic equations at an axial inflow/outflow boundary:

$$\frac{\partial C^-}{\partial t} - (vz - a)\frac{\partial C^-}{\partial z} = 0, \quad (3.62)$$

$$\frac{\partial C^+}{\partial t} + (vz + a)\frac{\partial C^+}{\partial z} = 0 \quad (3.63)$$

where:

$$C^- = vz - \frac{2a}{\gamma - 1}, \quad C^+ = vz + \frac{2a}{\gamma - 1} \quad (3.64)$$

These boundary condition equations are based upon an inflow inlet and an outflow exit. Aerodynamic conditions not satisfying these requirements (e.g., reverse flow) will cause spurious results or failure. In order to efficiently process boundary information in the numerical solution, phantom cells are located just outside the computational domain to permit the unmodified application of the interior point scheme at near boundary cells.

For subsonic normal inflow, the total pressure, total temperature, and flow angle are specified. The upstream running invariant C^- is extrapolated to the inlet, and the equation of state and flow equations are used to determine the variables at the inlet boundary.

At the exit, a static pressure is specified at the hub for internal flows, and at the outer boundary for external flows. The remaining pressures along the outflow boundary are calculated by integrating the radial momentum equation:

$$\frac{\partial p}{\partial r} = \frac{\rho v_{\theta}^2}{r} \quad (3.65)$$

In this case, the downstream running invariant C^+ is used to update the phantom cells at the exit boundary. Far-field boundaries also use this characteristic technique based on whether the local flow normal to the boundary passes into or out of the domain.

For applications where core flow conditions are simulated (e.g., combustor, high pressure spool device) boundary conditions similar to those just discussed are employed. The entrance to the core region is treated as a local exit of the domain, even though the region can be inside the computational domain. An example of this is seen in Fig. 3.3. A specified hub static pressure, radial momentum equation, and

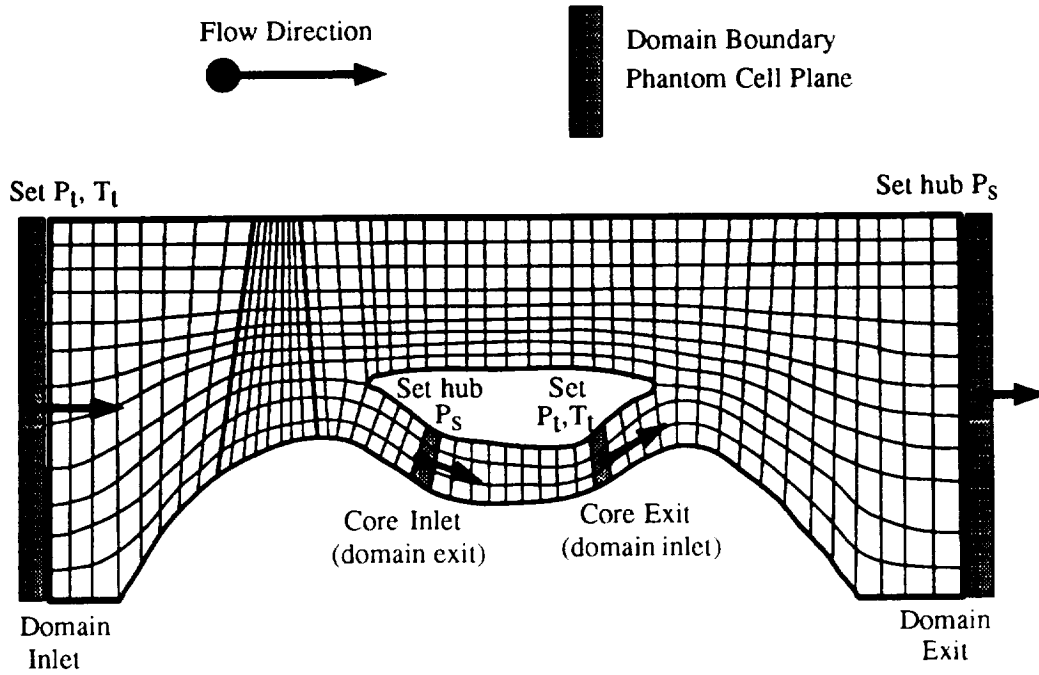


Figure 3.3: Computational domain highlighting core definition

characteristic equation set the flow variables. Similarly, the exit to the core region is treated as an independent inflow of the domain. Specified core flow total pressure, total temperature and flow angle are used with the characteristic equation to determine the flow quantities at the core exit boundary.

All solid surfaces (hub, cowl, radial flow splitters, and airfoils) must satisfy flow tangency for inviscid flow:

$$\vec{V} \cdot \vec{n} = 0 \quad (3.66)$$

or no slip for viscous flows:

$$v_z = 0, \quad v_r = 0, \quad v_\theta = r\omega \quad (3.67)$$

In both cases, we specify no flux through the boundary (an impermeable surface), and hence, only pressure is needed at the phantom cell. The pressure is determined by extrapolation. Solid surfaces are also assumed to be adiabatic, which implies that the normal temperature gradient is also zero.

The calculation presumes that the flow solution is periodic with a period of one pitch (arclength between tangential extrema of the grid). Therefore, all cells at the tangential boundaries of the domain (and not defining a solid surface) take as their phantom cell flow variables the quantities from the cell volume at the opposite tangential bound.

3.9 Solution Procedure

A procedure for obtaining a numerical solution for multiple blade rows is described below. The single blade row case is in general a reduction of the multiple blade row case and is described later. Before executing the solution algorithm, numerical grids (one for each blade row) are required. These grids model the actual three-dimensional geometry of their particular blade row, and represent the rest of the domain as an axisymmetric duct. The average passage method requires all grids to have the same meridional representation (i.e., the same dimensional (z,r) coordinate lattice structure). More information on the required grids can be found in [9].

Once the grids are obtained, the solution procedure is begun from a specified initial condition. This initial condition is a uniform flow, or is introduced from a previous solution. The multiple blade row solution is found using a nested iteration procedure with an inner and outer loop as seen in Fig. 3.4. Within the inner loop, the Runge-Kutta time integration is used and the Euler/Navier-Stokes equations are solved for a particular blade row (grid). As mentioned earlier, the average passage form of the equations are used and the neighboring blade row effects (blade forces, correlations) are modeled as steady parameters for the inner loop time integration. When each blade row in the domain has gone through this iteration and the blade row effects have been recalculated, one cycle or “flip” through the system (outer loop) is complete. Once during a flip, each blade row’s force terms are updated based upon the the axisymmetric average of that blade row’s flow field. When these updated effects are used depends upon user control of the solution procedure. For Fig. 3.4 the neighboring blade row effects are all from the previous flip. However, if the updated terms for the current flip are used, the solution procedure is represented in Fig. 3.5. For more information on solution procedure techniques see [10]. Solutions are deemed converged when the average residual R has been reduced by a factor of 10^{-3} .

For a single blade row case, the solution procedure is greatly simplified. With no neighboring blade rows and their effects to calculate, there is no outer loop. The Runge-Kutta time integration for the equation system of the single blade row is executed until the convergence criterion is met.

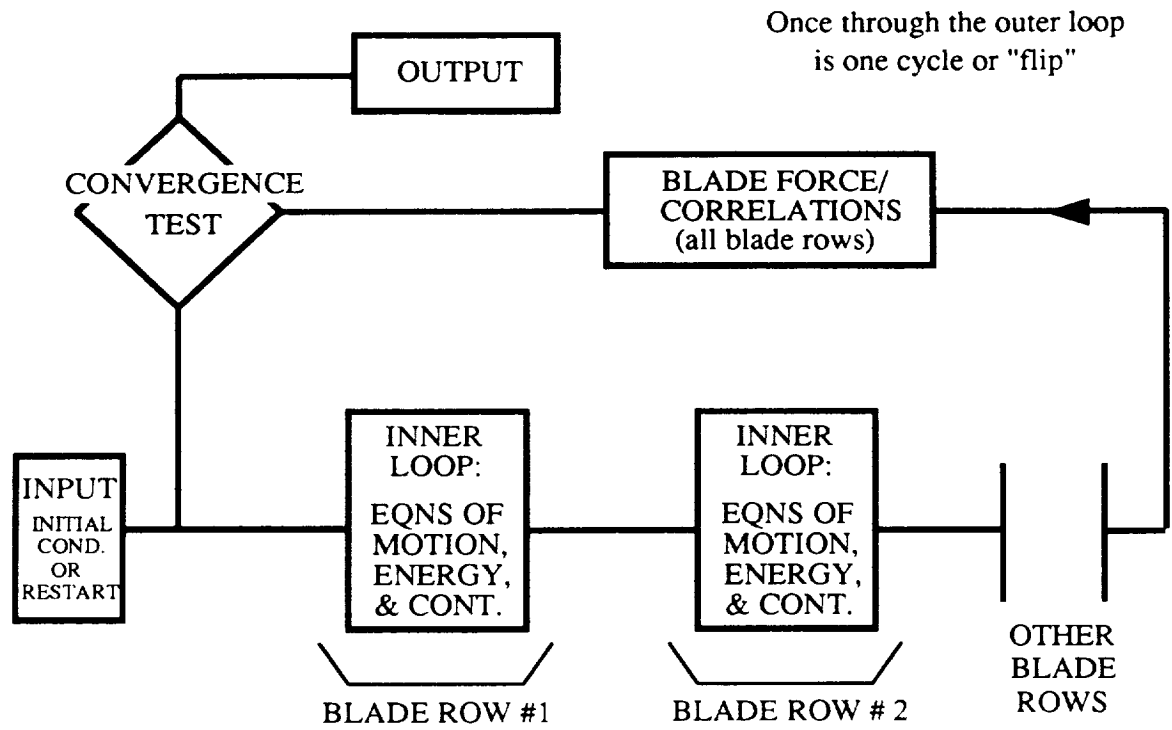


Figure 3.4: Multiple blade row solution procedure

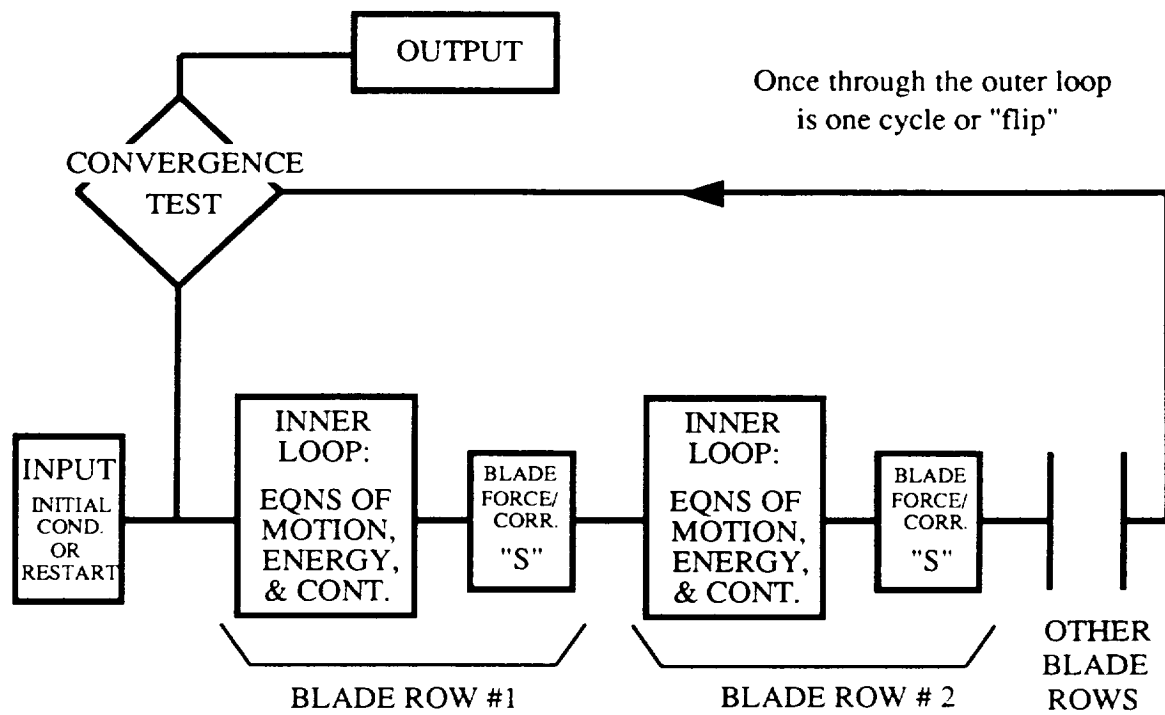


Figure 3.5: Solution procedure using updated blade row effects

4. RESULTS

In the following sections, solutions from the computational procedure described in the previous chapter are presented. An Euler solution for the fan section of the GMA 3007 will be presented and compared to experimental data. Also, an Euler solution for the GE/NASA Energy Efficient Engine (E cubed) fan section will be shown. Following this, a flat plate test case showing the boundary layer characteristics predicted by the Navier-Stokes algorithm will be presented. Finally, comparison of a viscous solution for the GMA 3007 fan section to experimental data will conclude the chapter.

4.1 GMA 3007 Fan Section - Euler Analysis

The initial verification of the original Euler flow solver was presented in [1] and the solver has essentially remained the same since then. To test the multiple flow splitter capability, calculations were done on the geometry of the GMA 3007 fan section. The simulation of the fan section included the rotor, the core duct guide vane, and the bypass duct guide vane. One radial flow splitter (the core/bypass duct splitter) is part of the geometry, and this splits the exit of the computational domain. All these features can be seen in Fig. 4.1 which shows an axisymmetric plane of the

Table 4.1: Grid parameters for the GMA 3007 geometry

Blade Row Grid	Streamwise Points	Spanwise Points	Tangential Points	Blade Pts LE to TE	Blade Pts Hub to Tip
Fan Rotor	101	29	15	21	29
Core Duct Vane	101	29	11	13	17
Bypass Duct Vane	101	29	11	17	17

computational grid. The full grid consists of 101 streamwise points, 29 spanwise points, and 15 tangential points. Some sections of the full grid for the rotor are shown in Fig. 4.2. Both the core vane and bypass vane grids are (101X29X11). Table 4.1 shows pertinent statistics for the grids used. The grid does not model the rotor tip clearance region.

Test data for this geometry was available and Fig. 4.3 displays the locations where data was taken on a schematic of the fan section. The data consisted of total pressure and temperature measurements taken at the leading edges of both vane rows and at radial rakes downstream of the vanes.

The fan section was simulated with the rotor at design speed. Converged solutions were obtained for different total pressure ratios by setting the exit static pressure condition. The performance characteristic (mass-averaged total pressure ratio vs. mass flow) of these solutions is compared to the experimental values in Fig. 4.4. The Euler solutions consistently over flow at this rotor speed and this is primarily caused by the lack of boundary layer blockage on the blade row surfaces. At the highest pressure ratio condition (near stall) the difference in mass flow is greatest and again this is not atypical of inviscid analyses. The shock-boundary layer interaction

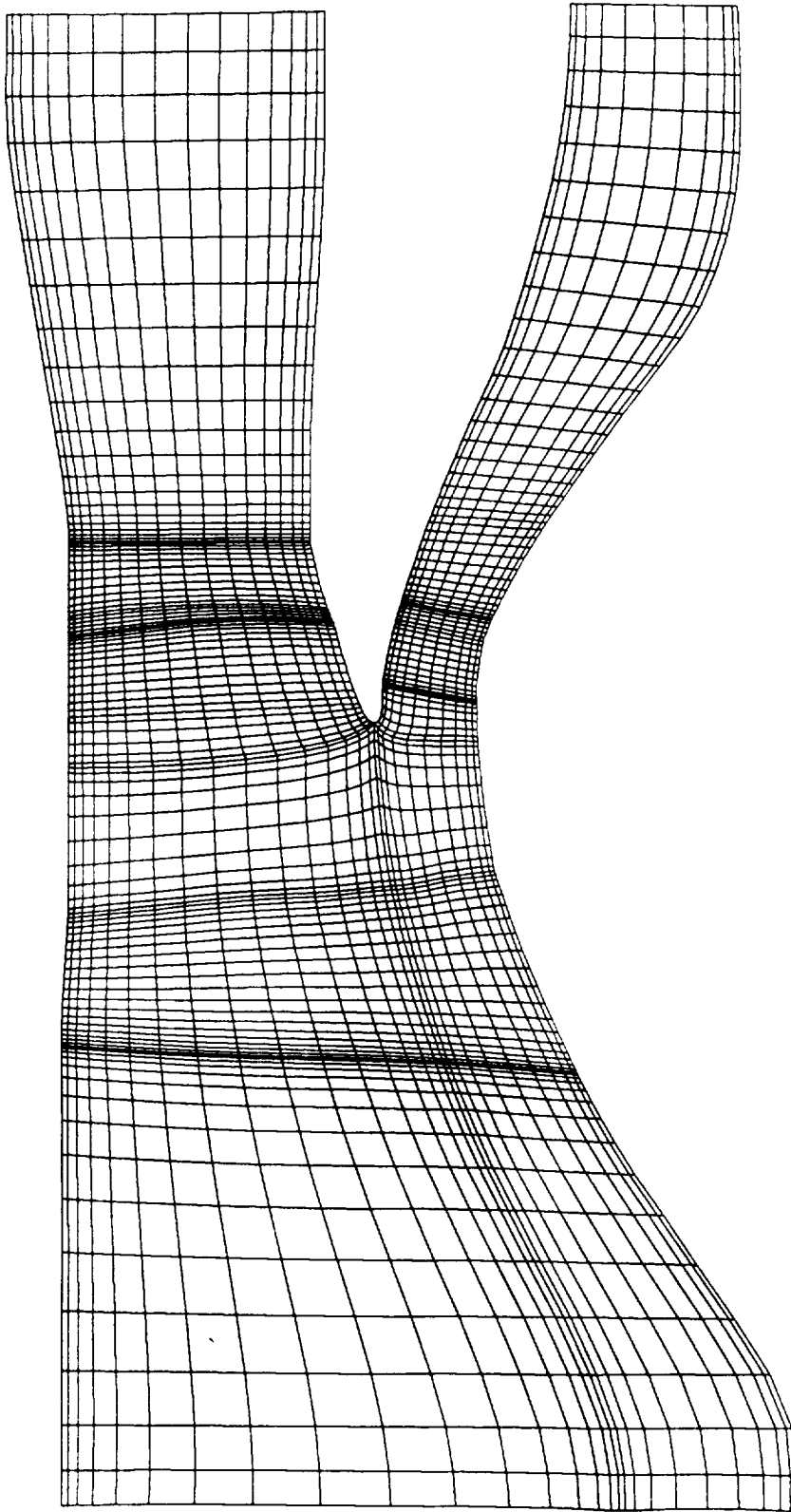


Figure 4.1: Axisymmetric plane of GMA 3007 Euler grid

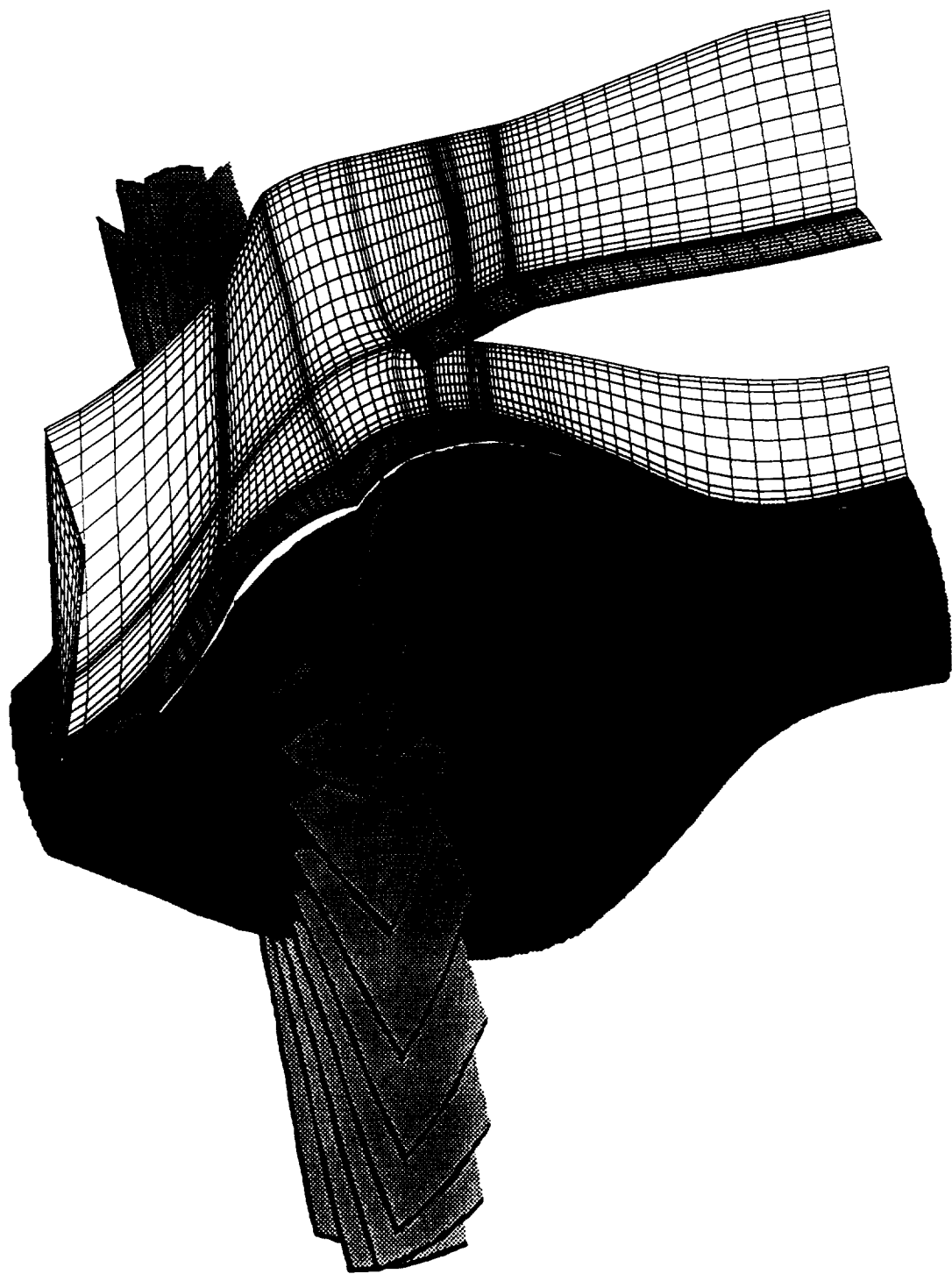


Figure 4.2: 3-Dimensional grid for GMA 3007 rotor grid

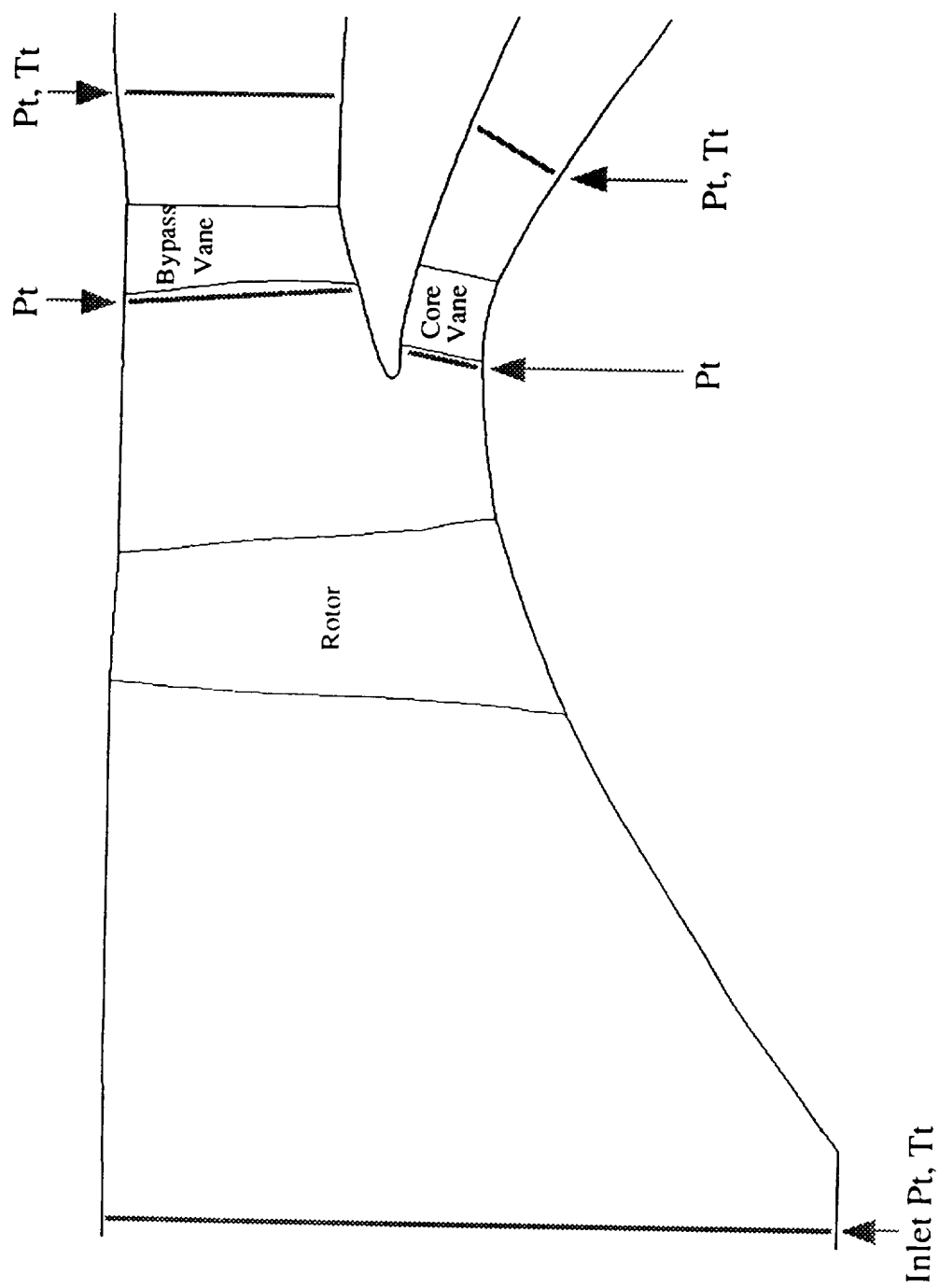


Figure 4.3: GMA 3007 experimental measurement location schematic

which usually has a significant effect on the performance of a highly loaded blade row is not modeled in these solutions.

Mass-averaged radial profiles of total pressure ratio are shown for two operating conditions of the fan section in Fig. 4.5. The pressure ratios are compared at the Rotor Exit Plane which is seen in Fig. 4.3. No data was actually taken at this plane and the test data shown in Fig. 4.5 has been back calculated from the vane leading edge locations based on predicted streamlines. Comparing results at the true data locations shows the same characteristics seen in Fig. 4.5. For both conditions, the Euler solution produces more pressure ratio in the lower portion of the span and less pressure ratio in the upper portion, with this discrepancy decreasing at the near stall condition. However, it should be noted that several Navier-Stokes analyses have been run on this fan section and all show more pressure rise near the hub than that seen in the test data. A potential explanation is that there is an error in the test data. The discrepancy in the upper portion of the span can be related to low grid resolution, the lack of a tip clearance model, and the inability of the inviscid solution to accurately model the boundary layer effected shock behavior in the blade passage.

Figure 4.6 compares predicted and measured efficiency profiles at an operating condition near the design point. While the Euler solution's mass-averaged efficiency is similar to the test data, the radial profile is significantly different. Part of this difference is likely due to the inviscid analysis's lack of a model for end wall and tip clearance losses.

Static pressure contours for the rotor flowfield are shown in Fig. 4.7. Pressure is displayed on the solid surfaces of the rotor grid and the blade surface pressure for the

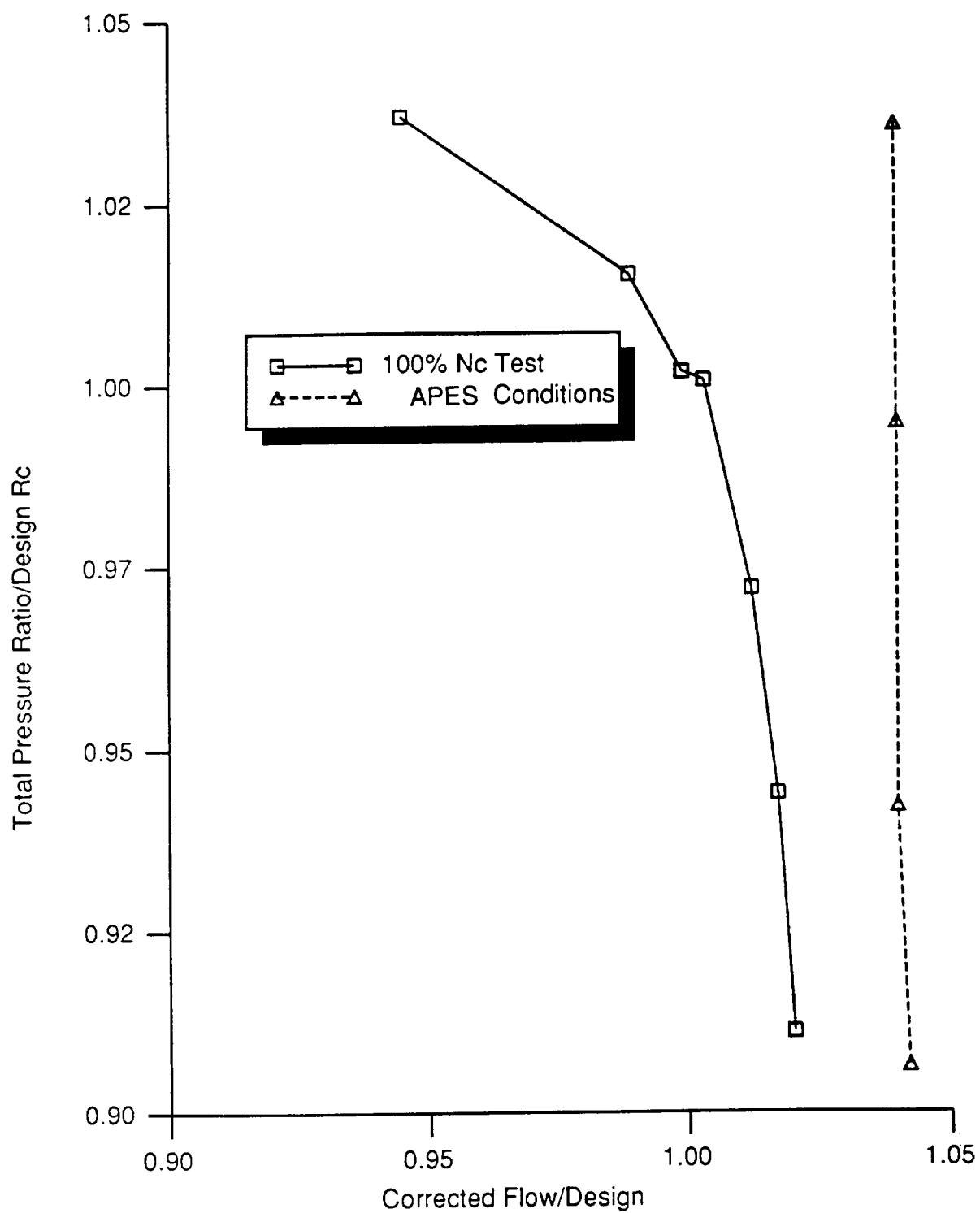


Figure 4.4: GMA 3007 design speed characteristic

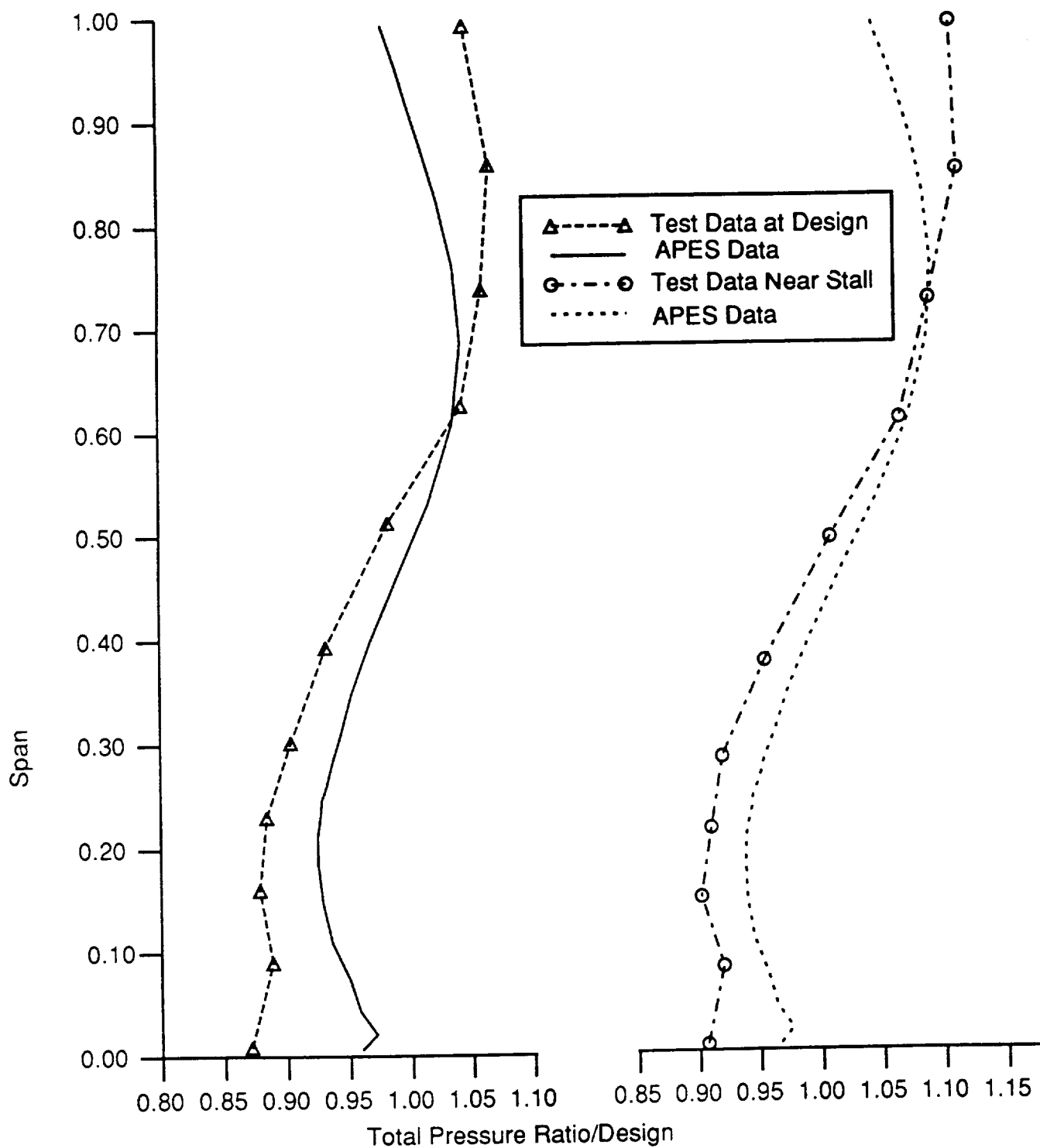


Figure 4.5: GMA 3007 Euler solution: total pressure ratio profile

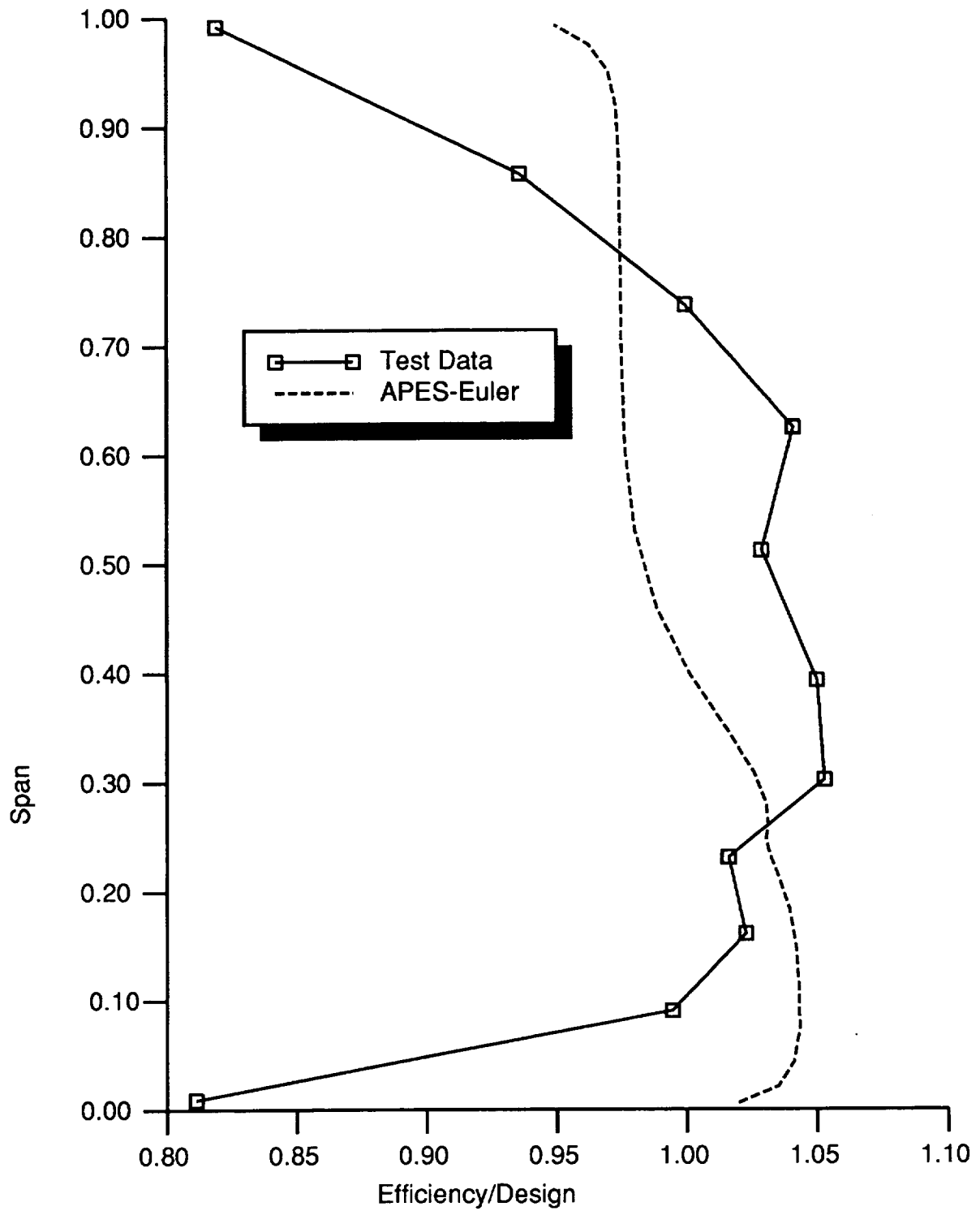


Figure 4.6: GMA 3007 Euler solution: radial profile of efficiency

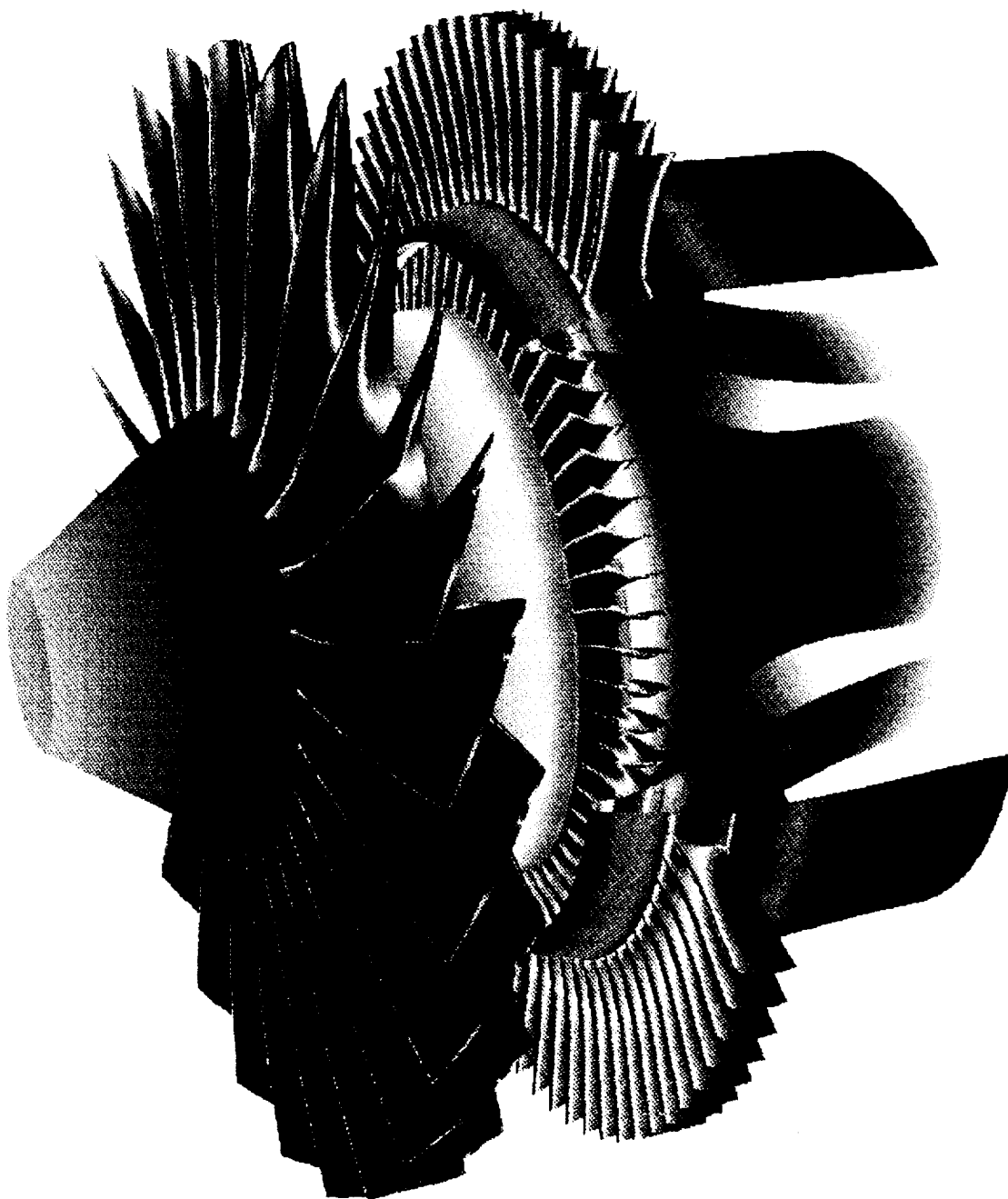


Figure 4.7: GMA 3007 Euler solution: color contours of static pressure

two vane rows are included as well. A portion of the core/bypass duct splitter has been removed to display more of the core vane row. The passage shock's termination on the rotor pressure surface is seen on the upper blades. The passage shock was in the aft portion of the blade row which is typical of inviscid simulations. The influence of the splitter on the rotor performance was not significant and that will be discussed further in a later section.

4.2 Energy Efficient Engine Fan Section

The flowfield about the GE/NASA Energy Efficient Engine (E cubed) fan section was also simulated to test the Euler version of *APES*. The geometry included the fan rotor, a booster stage, a core duct guide vane, and a bypass duct guide vane. The geometry can be seen in Fig. 4.8, which is an axisymmetric plane of the computational grid. There are three spanwise flow splitters. A core/bypass splitter breaks up the exit of the domain into two regions. There is an island splitter over the booster stage, and there is also a part span shroud which splits the flow on the fan rotor. The grid for each blade row has 185 streamwise points and 45 spanwise points. Table 4.2 shows pertinent statistics for the grids used.

This fan section geometry was tested and the reader is referred to [11] and [12] for details of the geometry and experimental configuration. The primary aerodynamic data taken was a performance map for the two air streams divided by the core/bypass duct splitter. For an operating condition near the design point, spanwise and tangential measurements were available as well as static pressures on the endwall surfaces. Figure 4.9 shows a schematic of the experimental measurement locations.

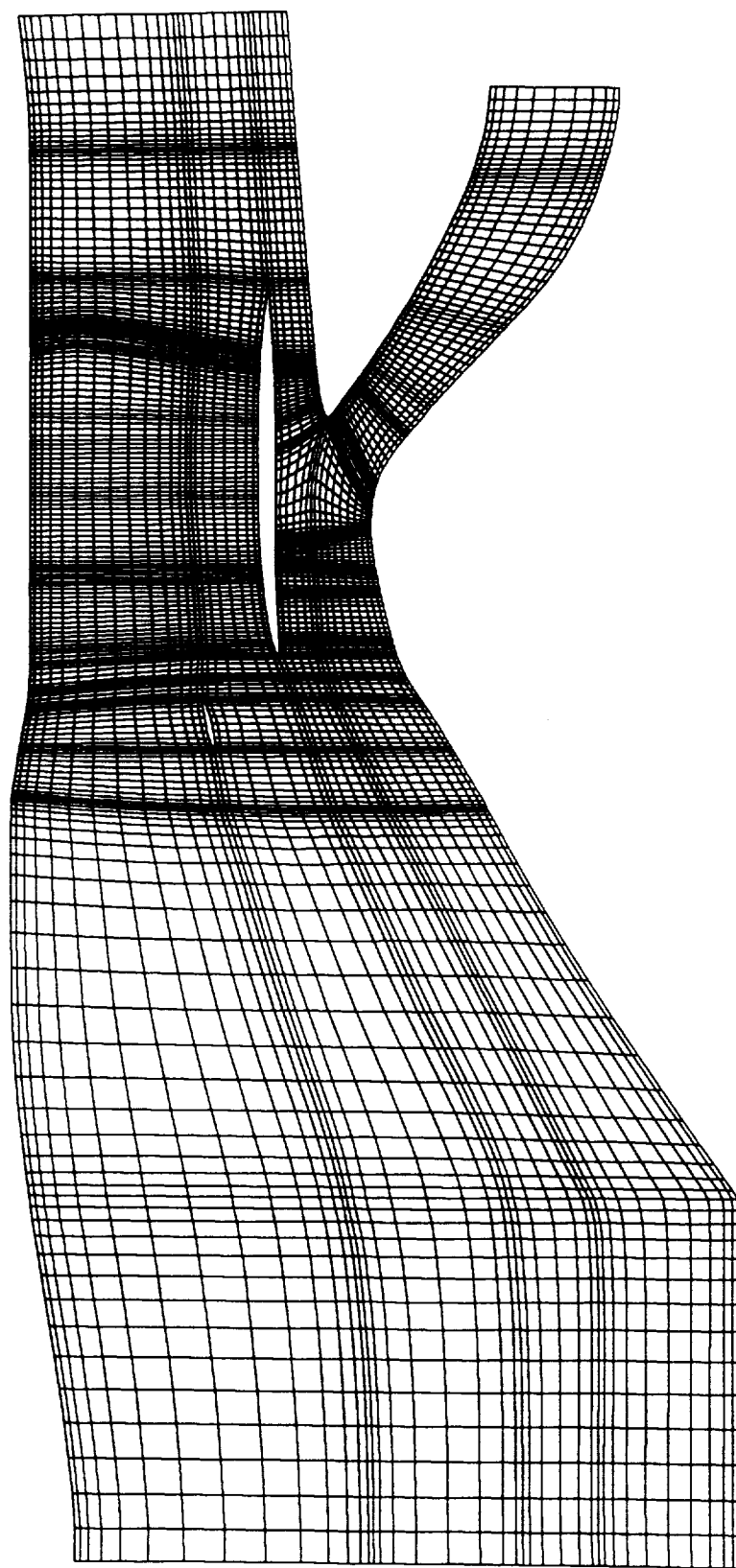


Figure 4.8: Axisymmetric plane of E cubed Euler grid

Table 4.2: Grid parameters for the E cubed geometry

Blade Row Grid	Streamwise Points	Spanwise Points	Tangential Points	Blade Pts LE to TE	Blade Pts Hub to Tip
Fan Rotor	185	45	15	29	45
Booster Stage Vane	185	45	11	15	19
Booster Stage Rotor	185	45	11	15	19
Core Duct Vane	185	45	11	13	11
Bypass Duct Vane	185	45	15	33	33

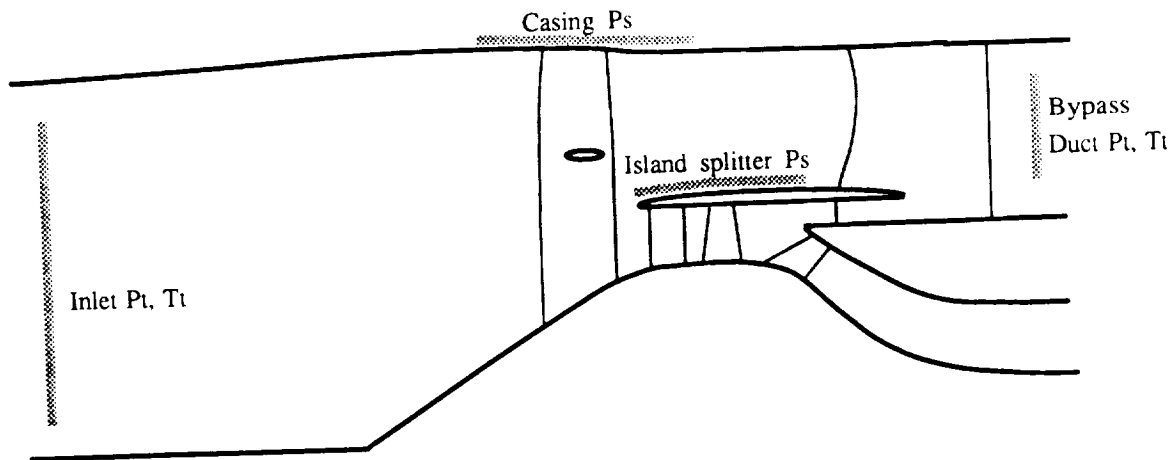


Figure 4.9: E cubed experimental measurement location schematic

A Euler solution was obtained at a condition near the design point and the mass-averaged performance for the flowfield is shown on the experimental data maps of Figures 4.10 and 4.11. The bypass duct value showed reasonable agreement with the experiment, with the solution overflowing by 2%. The core duct data showed significantly less mass flow than the experimental value. This discrepancy is due in part to the core vane row in the solution not representing the actual geometry. The core duct vane geometry was not available so an approximate model for the vane row was used.

Spanwise measurements were taken downstream of the bypass duct vane and this data is compared to the solution in Figures 4.12 through 4.14. Total pressure ratio is compared in Fig. 4.12 and the total temperature in 4.13. The range bars in the figures represent the variation in the stagnation quantity as recorded by the tangentially spaced arc rakes. The low values in the range are the wake measurements and the circle symbols represent mass averages of the arc rake data. Through much of the span, the comparison is reasonably good. However, at both endwalls deviations are apparent. The tip clearance flow not being modeled might be the cause of the discrepancy near the case. The missed performance in the core stream accounts for the differences seen near the splitter surface. The spanwise profile of efficiency is shown in Fig. 4.14. Again, the solution deviates from the experiment in the upper portion of the span and shows good agreement elsewhere.

Static pressure was measured on the case over the rotor and on the island splitter surfaces. A comparison of this experimental data to the numerical solution is shown in Fig. 4.15 and Fig. 4.16. For both the island splitter and the case, agreement is

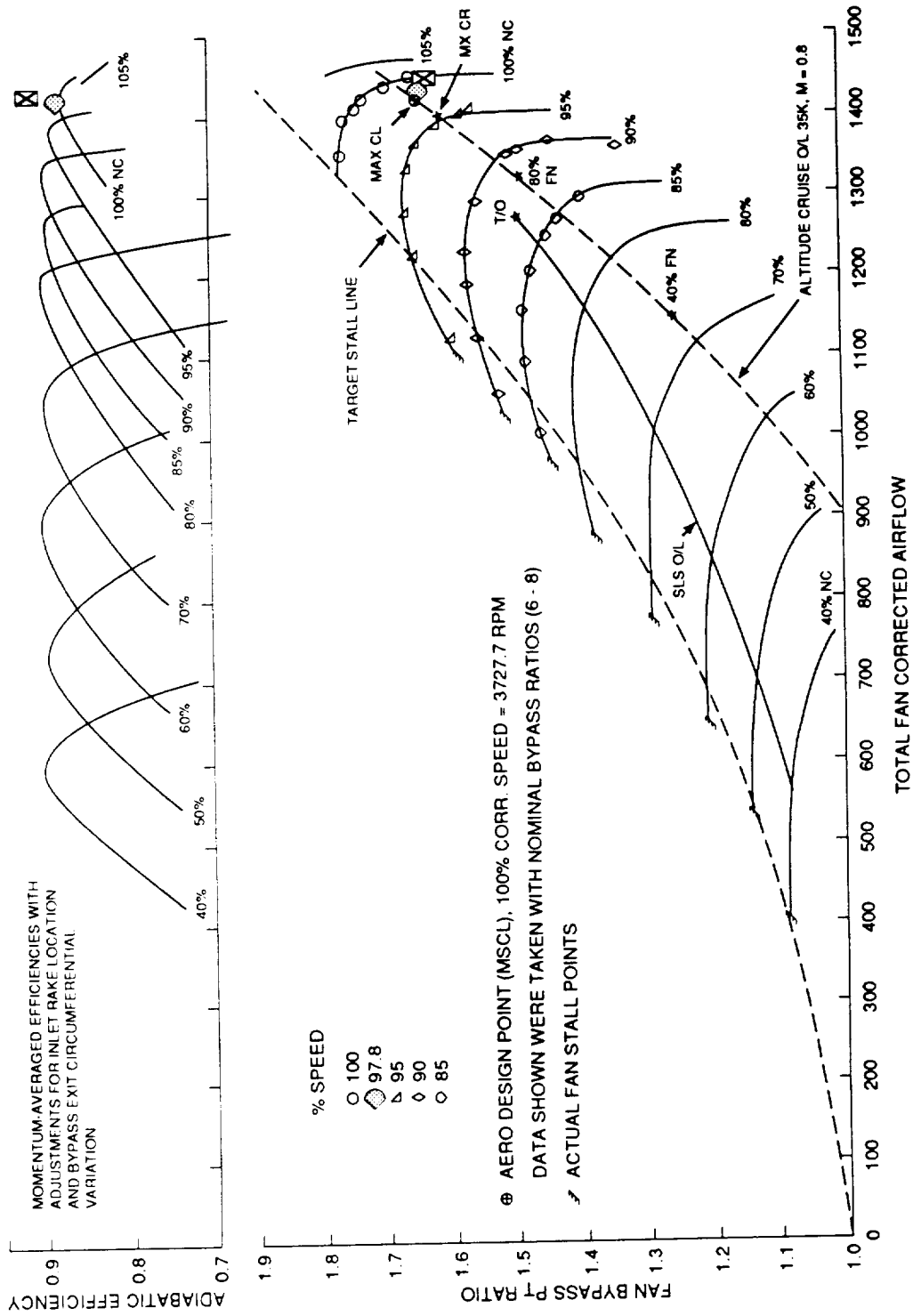
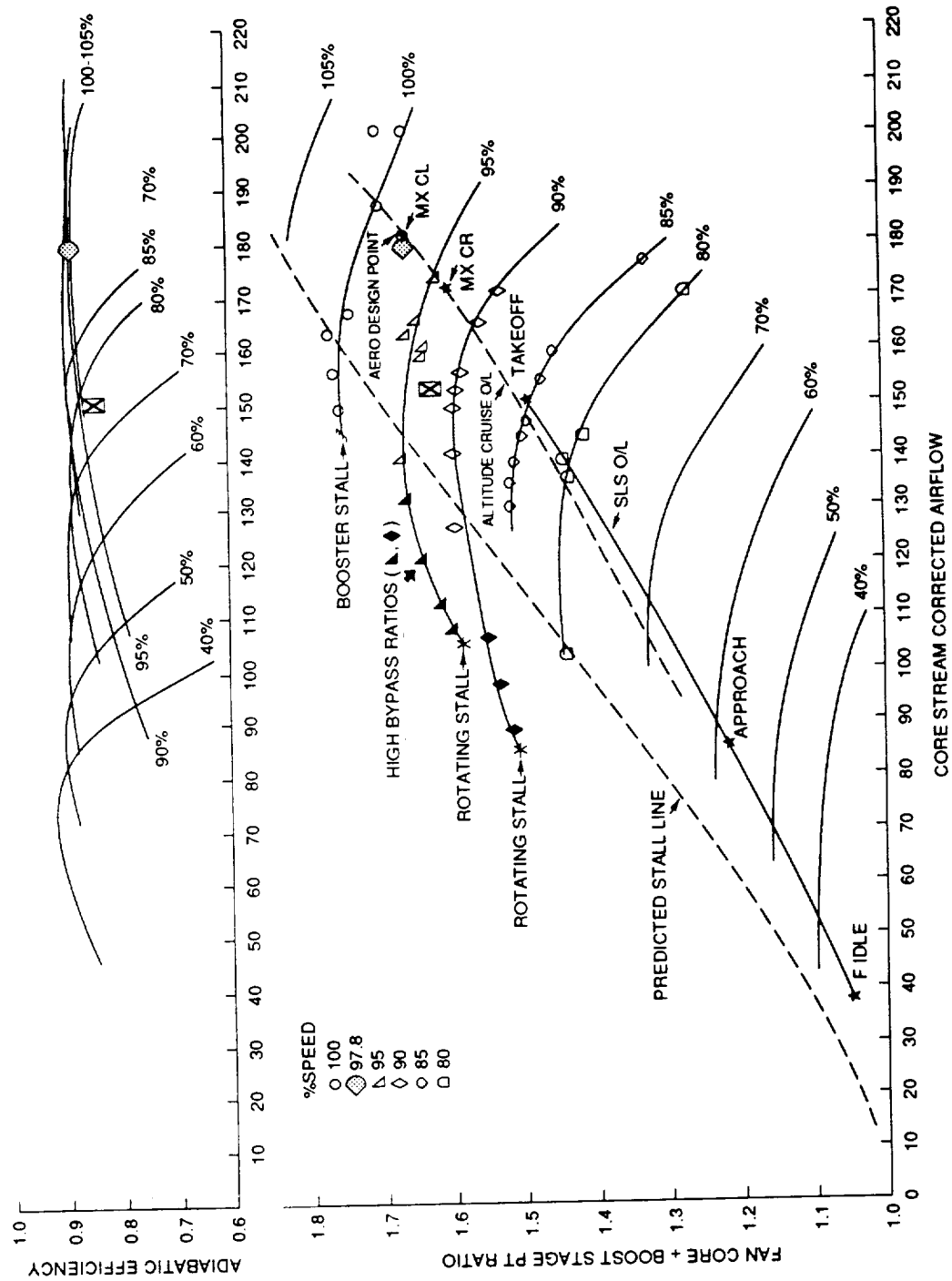


Figure 4.10: E cubed bypass stream performance map



TE92-3516-3

Figure 4.11: E cubed core stream performance map

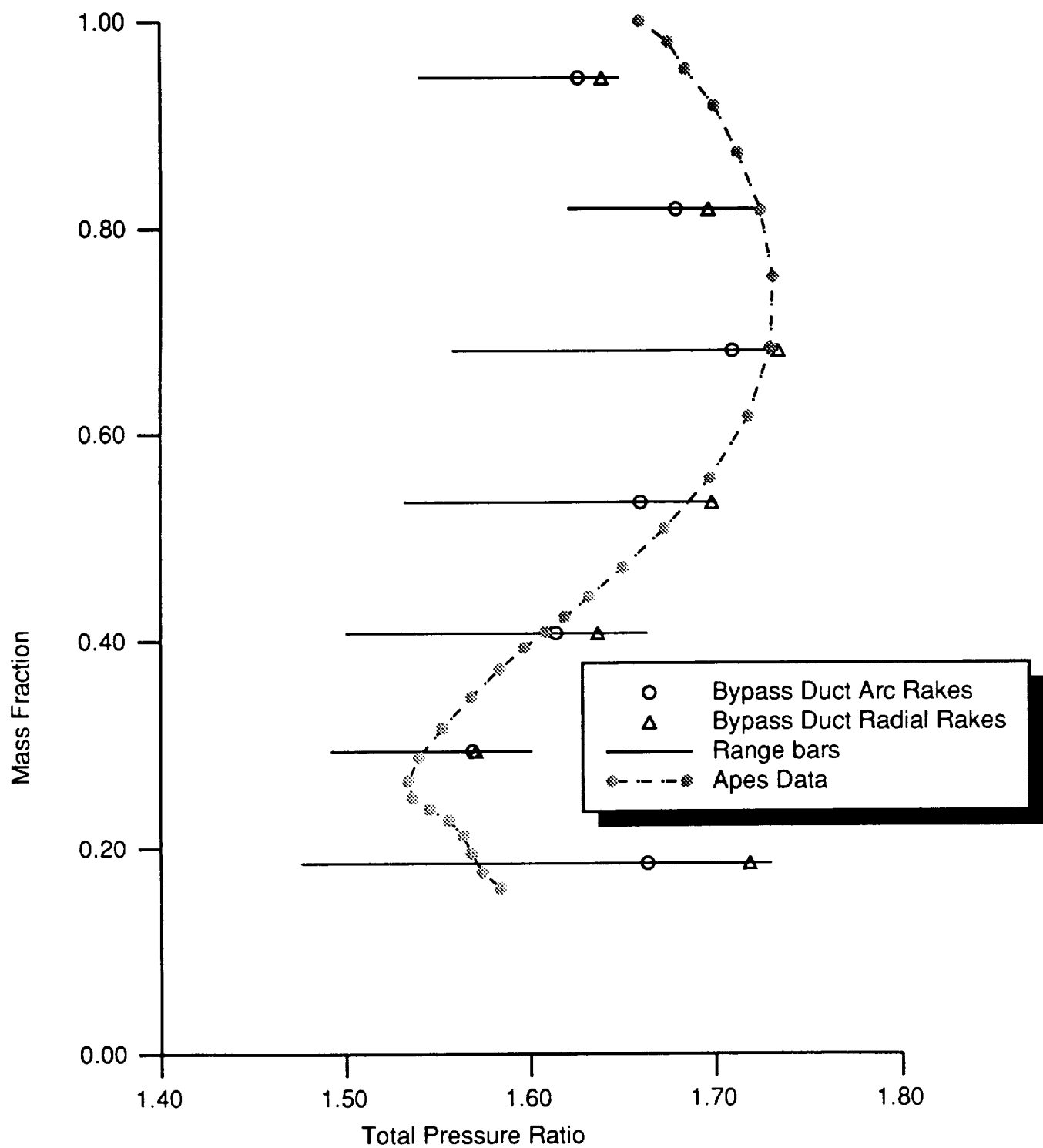


Figure 4.12: E^3 bypass stream total pressure ratio

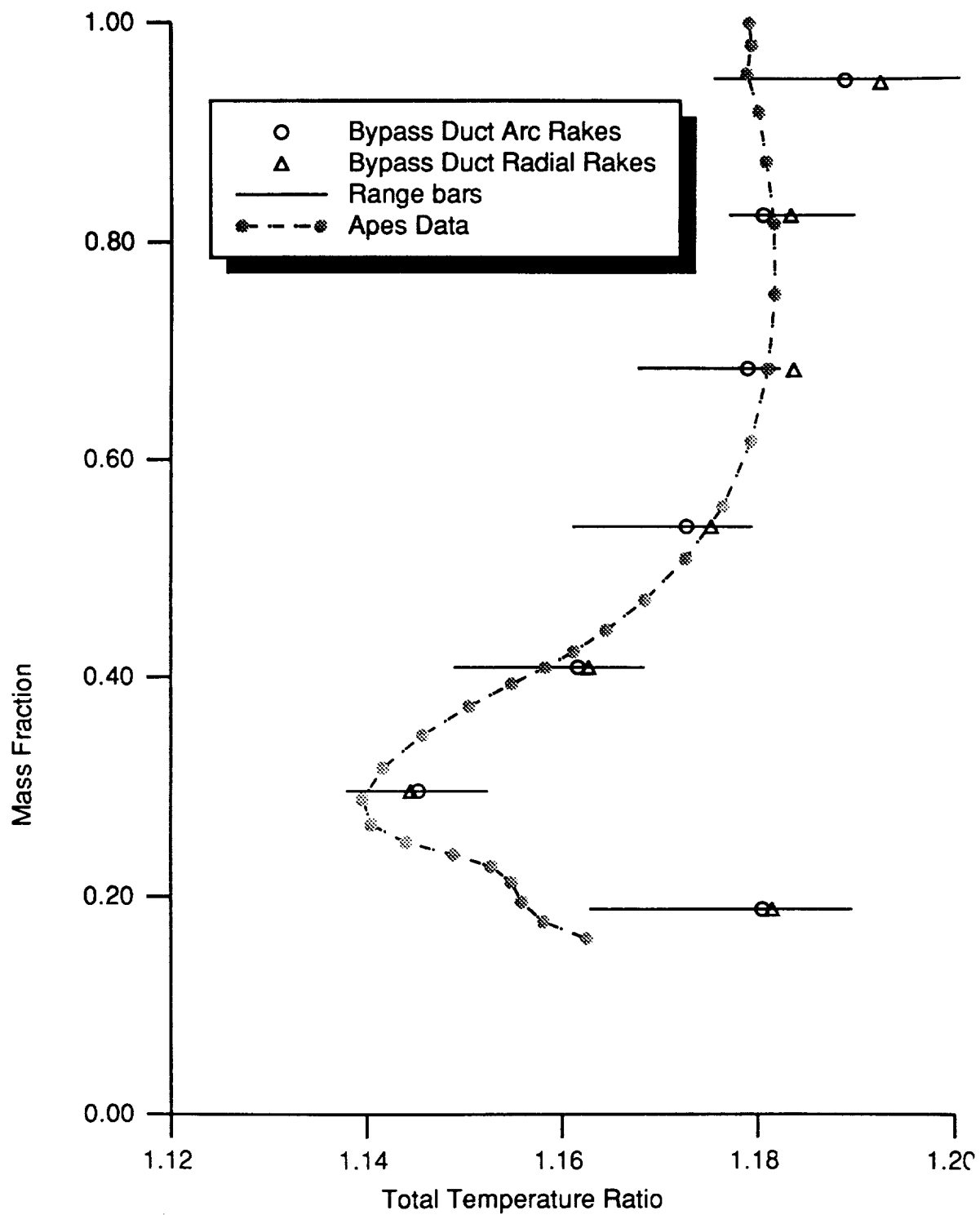


Figure 4.13: E^3 bypass stream total temperature ratio

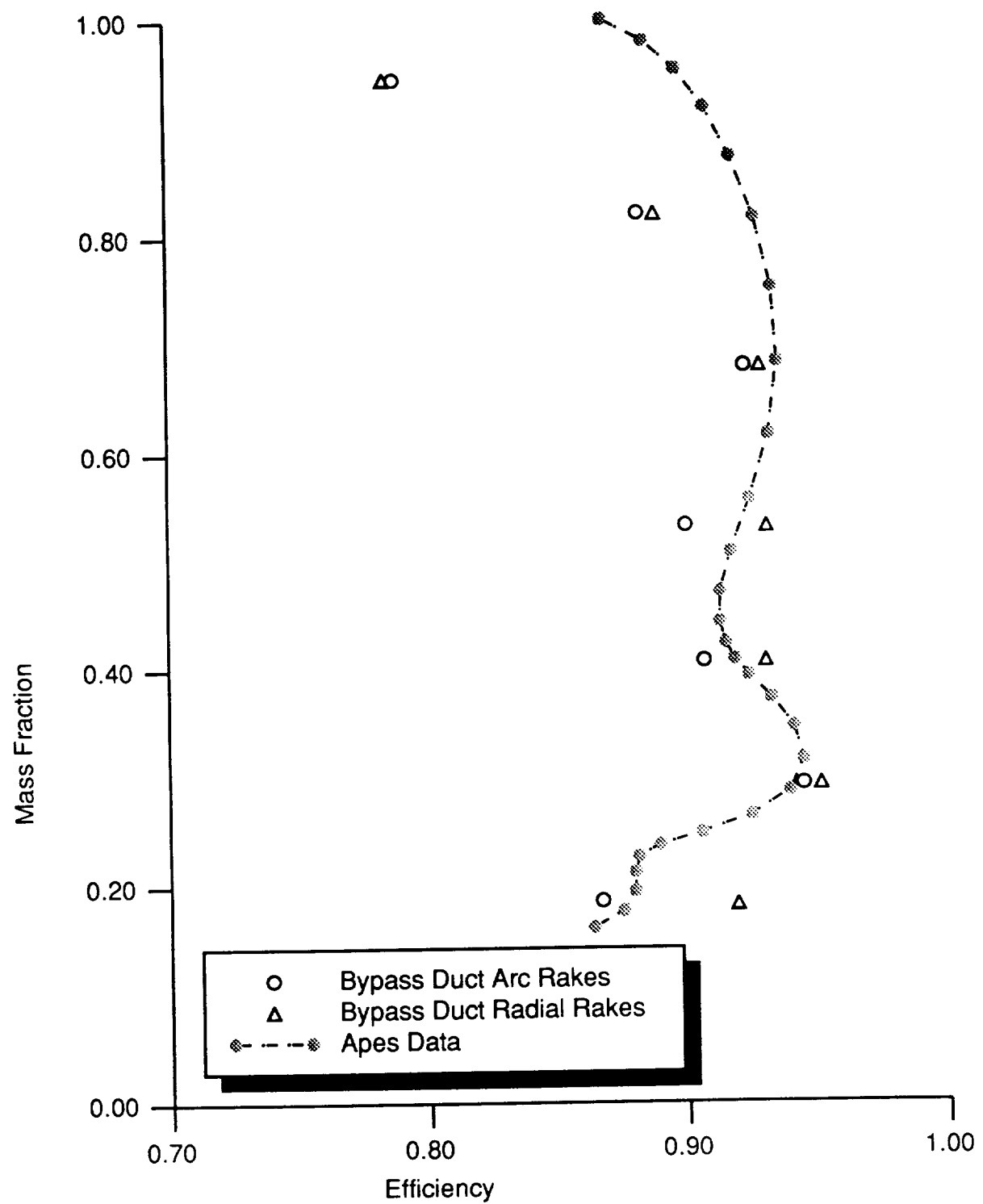


Figure 4.14: E cubed bypass stream spanwise efficiency

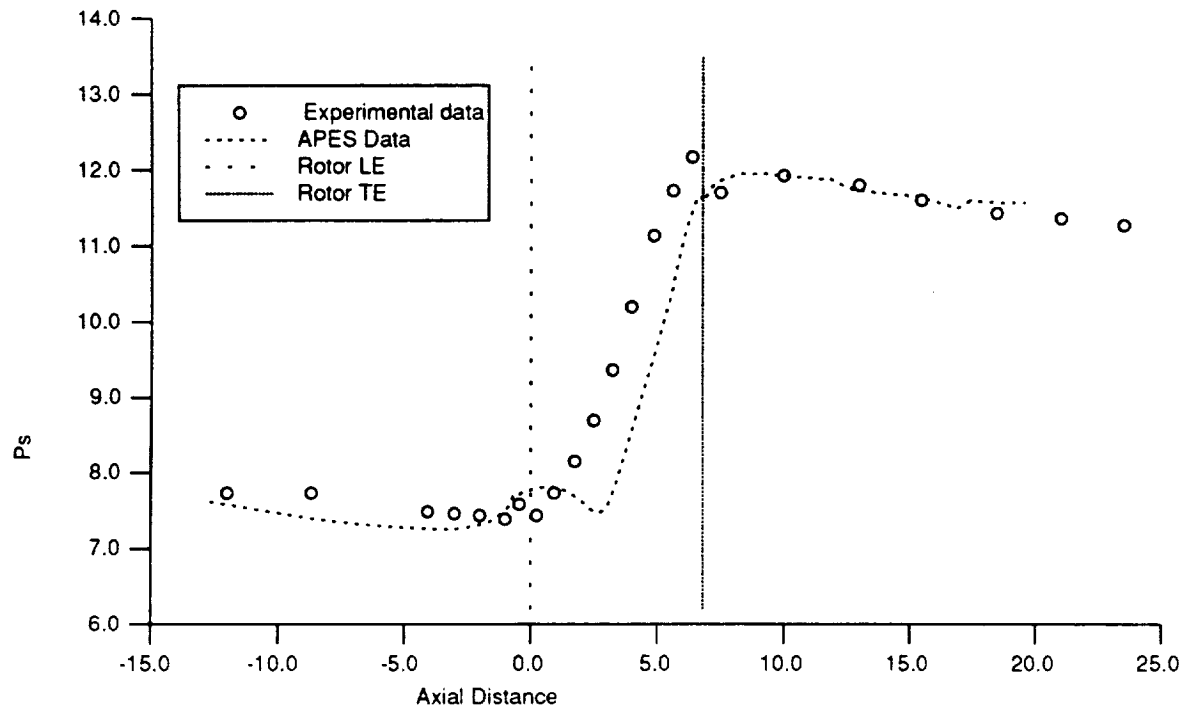


Figure 4.15: E cubed circumferential average static pressure: Casing

seen between the two sets of data. Only on the lower surface of the island splitter is a discrepancy shown, and this is probably due again to the mismatched core stream performance.

Static pressure contours for the numerical solution of the fan section are shown in Fig. 4.17. Isobar lines are portrayed near the suction and pressure surface with high pressure colored red and low pressure colored blue. The shock in the upper portion of the rotor is seen in the contour lines transitioning from green to red on each surface. The effect the part span shroud has on the flowfield is clearly seen in the figure.

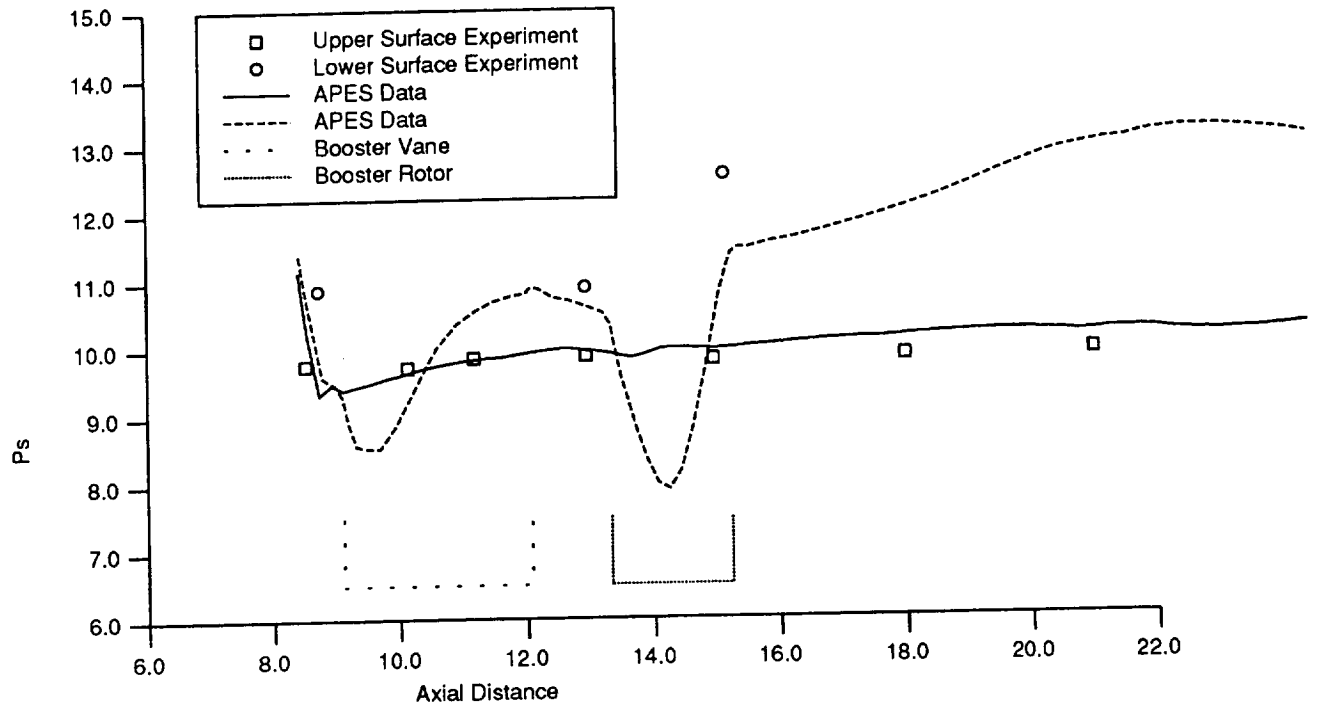


Figure 4.16: E cubed circumferential average static pressure: Island splitter

4.3 Navier Stokes Analysis of Flow Over a Flat Plate

To verify the boundary conditions and viscous terms modeled in the flow solver a laminar boundary layer was simulated. The simulated geometry was a cylindrical annulus with a large hub-to-tip radius ratio to minimize curvature effects. A zero thickness blade was aligned with the incoming flow, and the blade spacing set so that along the local blade surface at midspan, flat plate conditions were well approximated (i.e. the blades are far enough apart that there is little effect of the neighboring blade on the local boundary layer and midpitch can be thought of as a free stream or infinity condition). The grid had 73 axial points and 31 tangential points which were spaced so that at midchord of the zero thickness blade, ten points fell in the boundary layer.

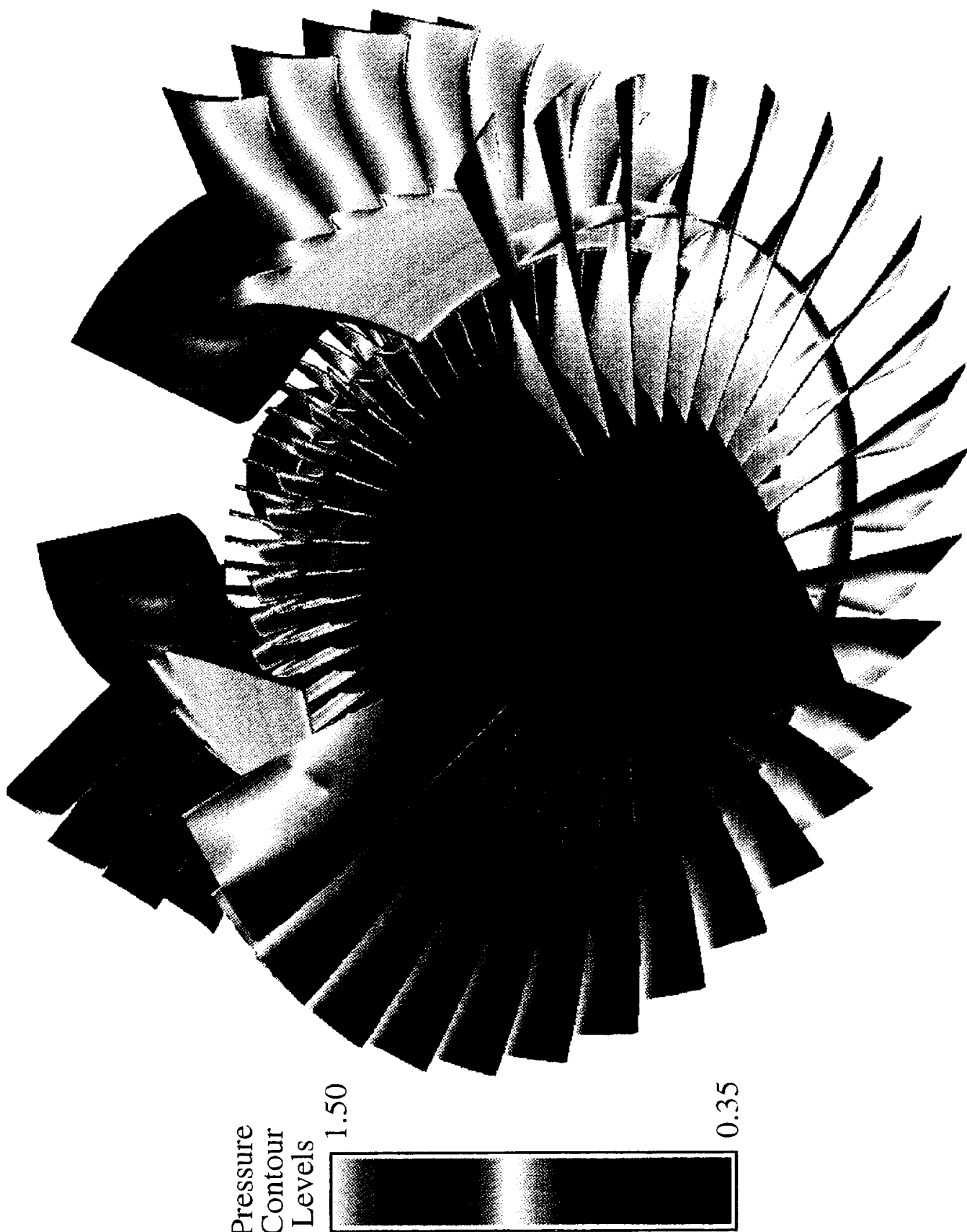


Figure 4.17: E cubed static pressure contours on solid surfaces

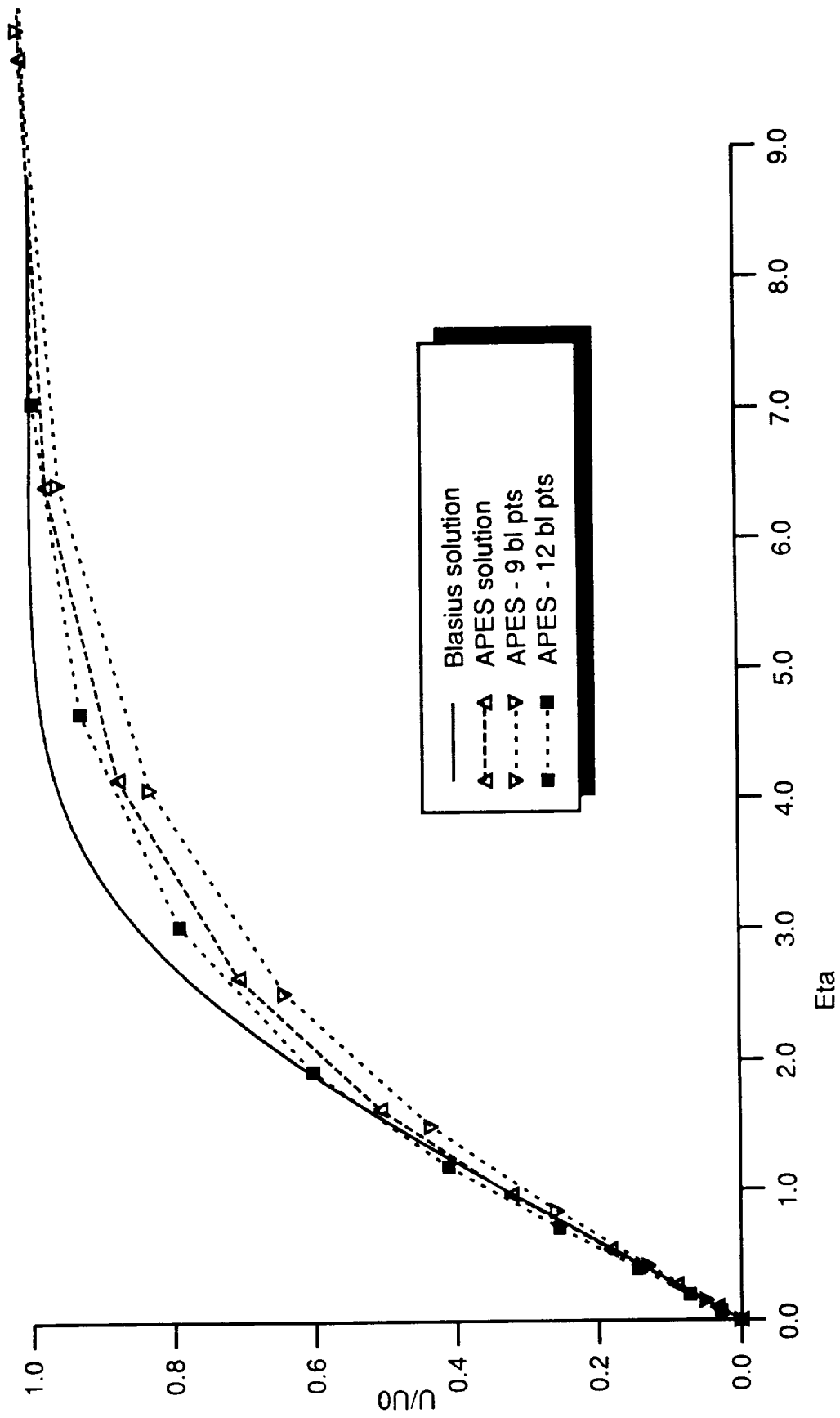


Figure 4.18: Laminar boundary layers on a flat plate

A laminar boundary layer solution was generated on the grid. The solution was compared to a Blasius solution for a boundary layer on a flat plate. A plot of the velocity distribution is shown in Fig. 4.18, and the two solutions compare fairly well. One region of disagreement is seen about η equaling 4, yet as the number of grid points in the boundary layer increases (from 9 to 12), the difference between experiment and numerical solution decreases.

4.4 GMA 3007 Fan Section - Navier Stokes Analysis

While most of the viscous flow solving capability of *ADPAC-APES* was taken from the original code [2] which was validated for turbomachinery flows, a verification of the multiple splitter modification was conducted. A Navier-Stokes analysis was done on the geometry of the GMA 3007 fan section. The geometry was the same as that of the earlier Euler analysis, which was the rotor and the core and bypass duct vanes. An axisymmetric plane of the computational grid is seen in Fig. 4.19. The full grid for the fan rotor is 141 streamwise points, 59 spanwise points, and 29 tangential points. The rotor grid models the tip clearance with seven points in the gap region. Both the core vane and bypass vane grids are (141X59X23). Table 4.3 shows pertinent statistics for the grids used.

The test data for comparison with the numerical solution is the same as that shown in the Euler analysis section and the reader is referred to Fig. 4.3 and that section for any details. The Navier-Stokes solution obtained was near the design point of the fan and was 1.4% higher in flow than the experiment (an improvement from 3.6% in the Euler solution).

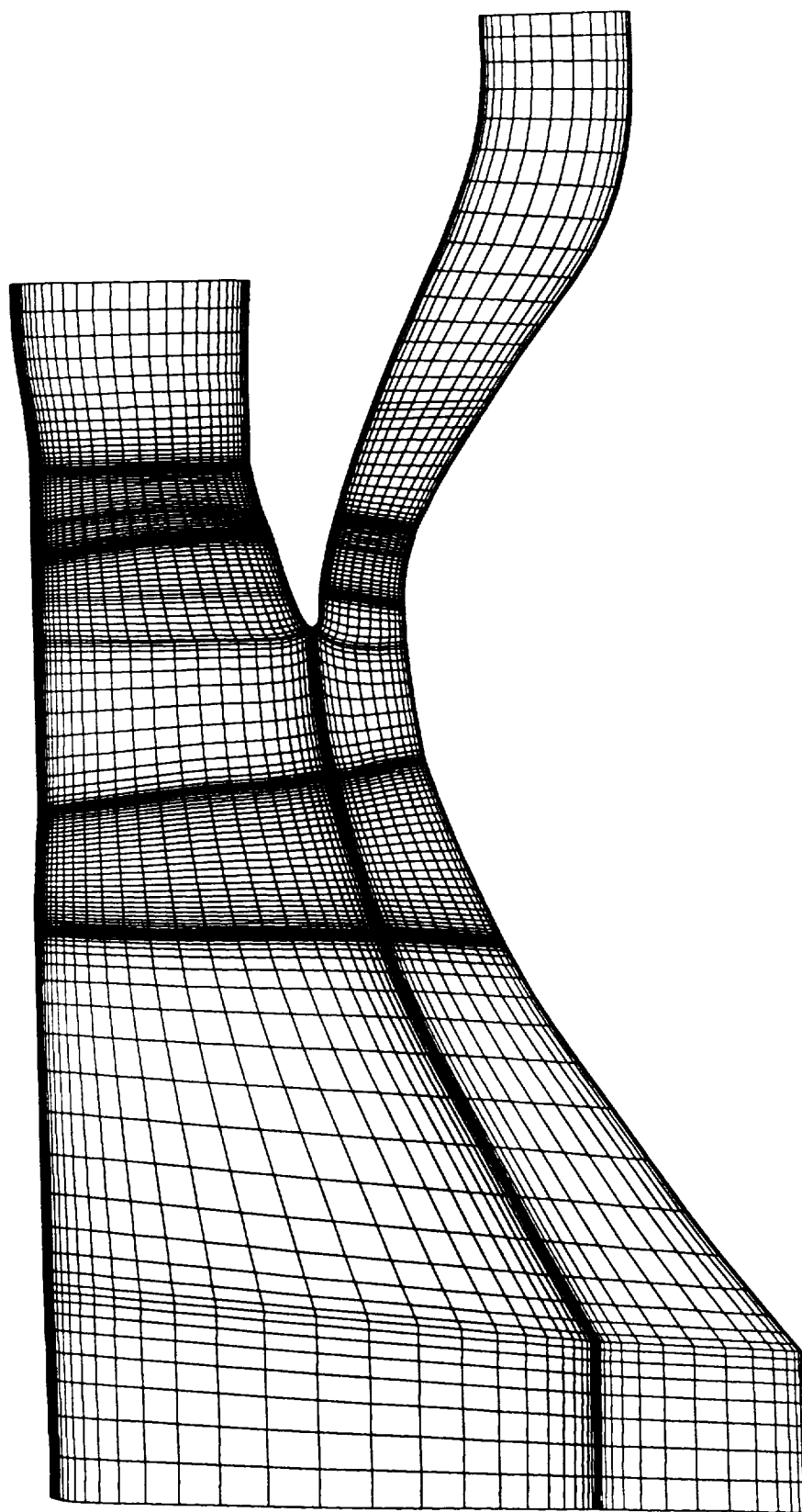


Figure 4.19: Axisymmetric plane of GMA 3007 Navier-Stokes grid

Table 4.3: Navier-Stokes grid parameters for the GMA 3007 geometry

Blade Row Grid	Streamwise Points	Spanwise Points	Tangential Points	Blade Pts LE to TE	Blade Pts Hub to Tip
Fan Rotor	141	59	29	35	53
Core Duct Vane	141	59	23	27	19
Bypass Duct Vane	141	59	23	29	39

Circumferential-averaged radial profiles of total pressure and temperature ratio are shown for the solution and the experimental data in Fig. 4.20. The two sets of data show good agreement at this fan condition. The solution compares much better to the experimental data than the Euler solution and this is probably due to several reasons. First, the boundary layer and other viscous phenomena are modeled in the Navier-Stokes solution. Also, the resolution of the grid is greater, and the tip clearance flow is modeled. Figure 4.21 compares efficiency from the experimental data and the numerical solution. Again, the viscous solution compares much better with the experimental data than the Euler analysis of Fig. 4.6.

An effect the tip clearance flow has on the numerical flowfield solution is shown in Fig. 4.22. The figure shows the tip region in the fan rotor flowfield. Contours of total pressure are shown on an axial plane just downstream of the rotor trailing edge. Red contours are the highest total pressure and blue contours are the lowest. Streamlines originating from the clearance region just above the blade tip are shown as black lines in the figure. Much of the tip clearance flow rolls up into a vortex and passes through the contour plane at a low total pressure region. The clearance flow clearly effects the local flowfield and its energy makeup.

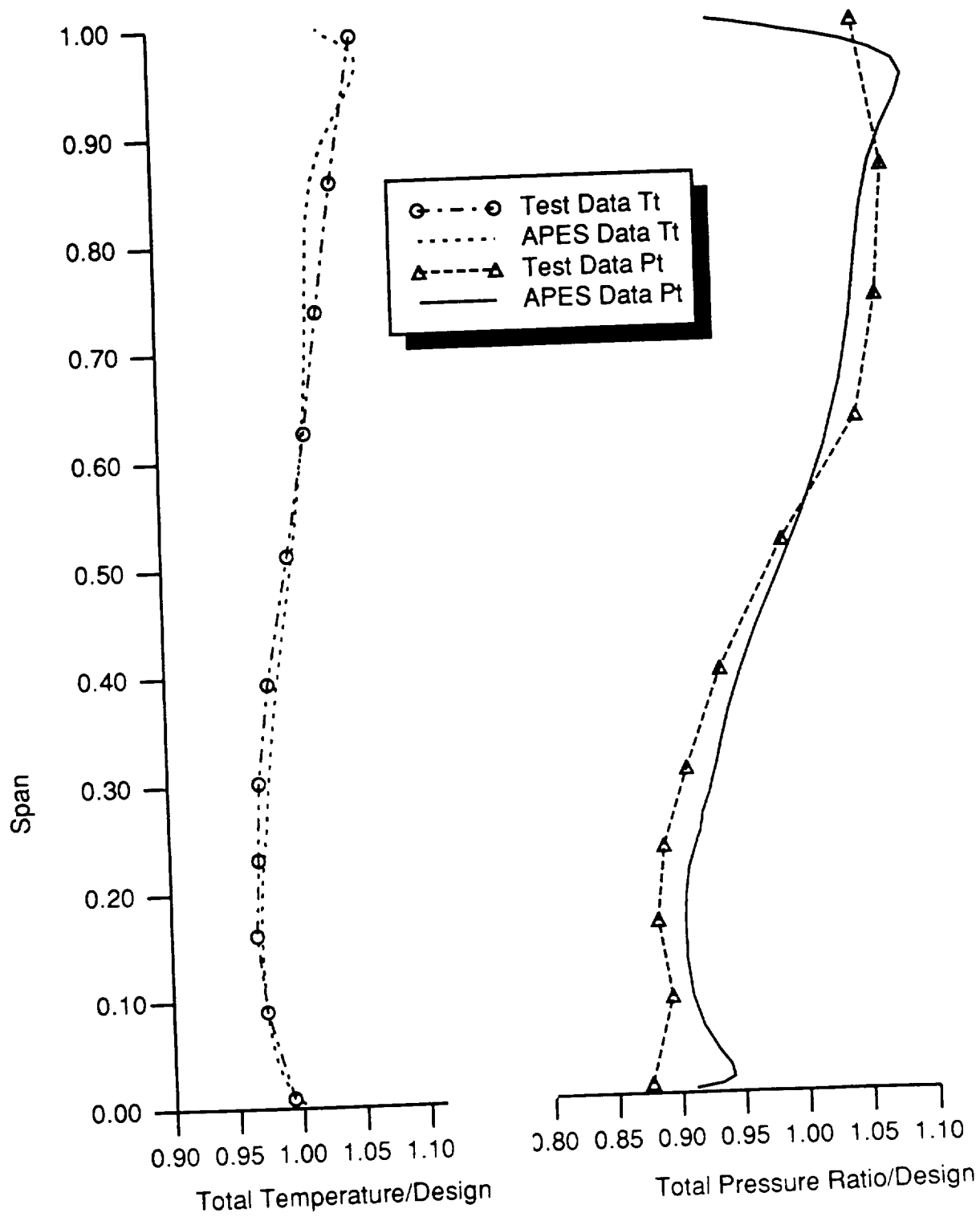


Figure 4.20: GMA 3007 Navier-Stokes solution: total pressure/temperature ratio profile

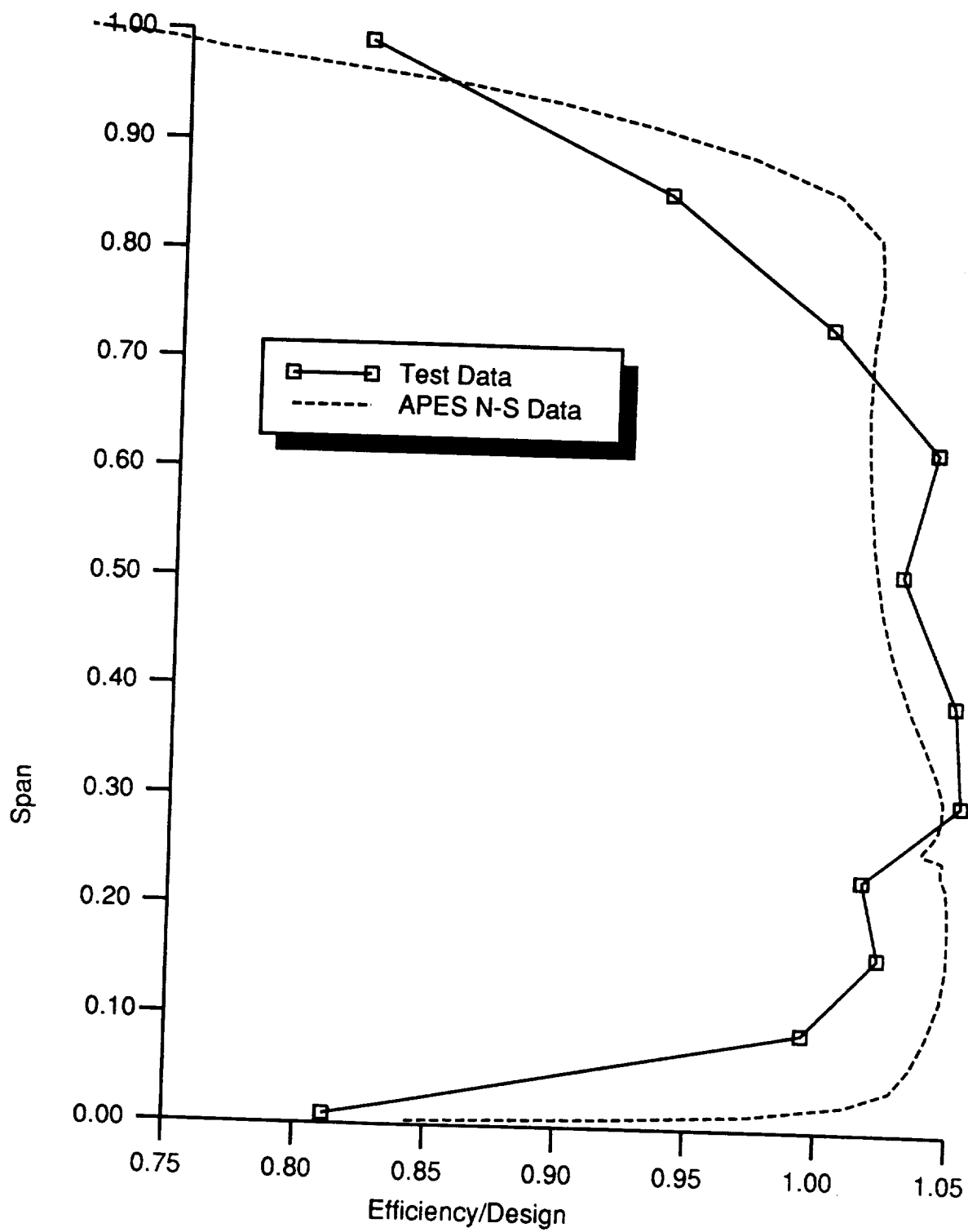


Figure 4.21: GMA 3007 Navier-Stokes solution: radial profile of efficiency

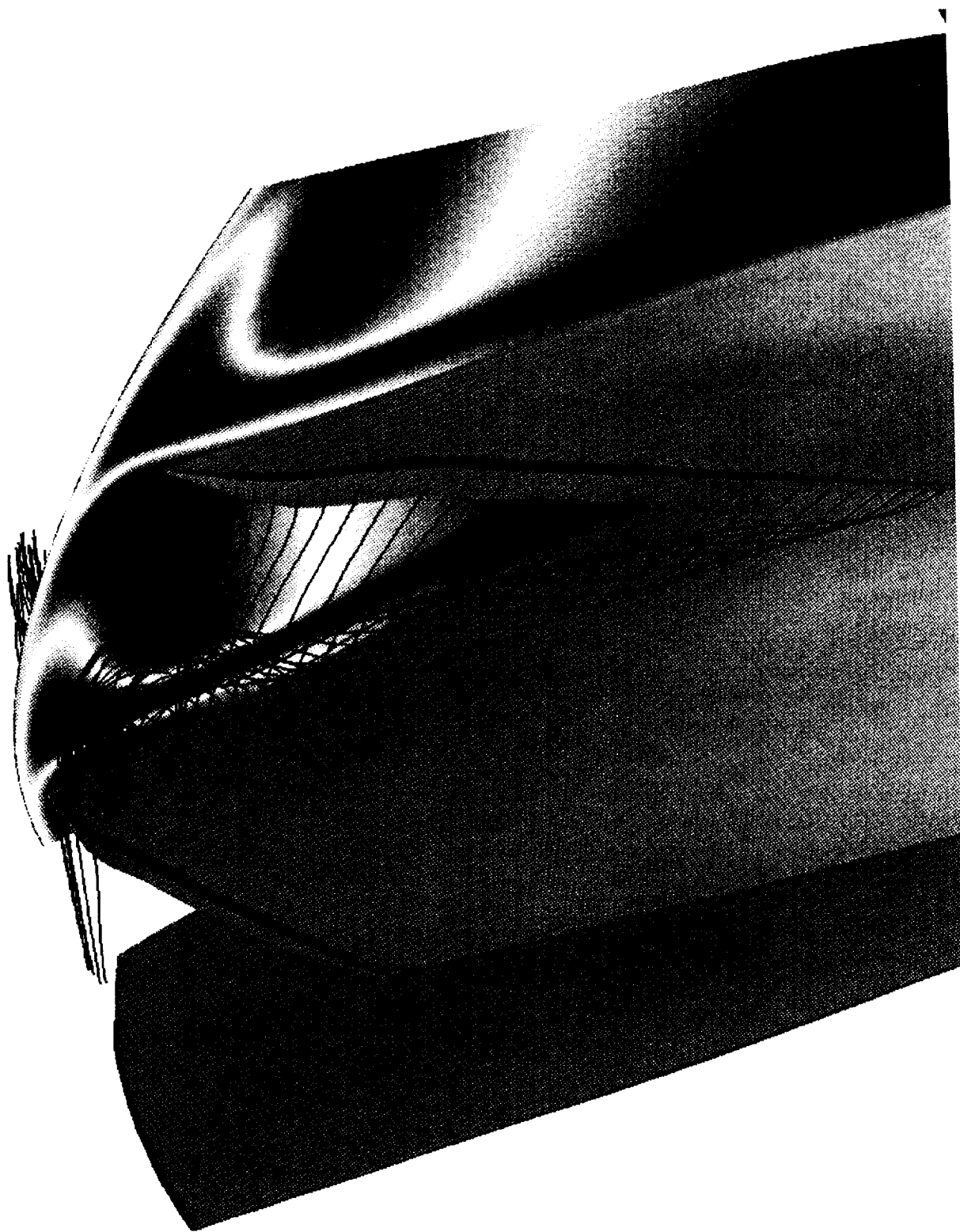


Figure 4.22: GMA 3007 Navier-Stokes solution: Tip clearance flow effects

5. CONCLUSIONS

A three-dimensional Euler/Navier-Stokes aerodynamic analysis has been developed (through modifying an existing analysis) for fan sections containing multiple radial flow splitters. The analysis is capable of calculating internal or external flows and can model engine core conditions. The analysis code was verified through comparisons with experimental data for two advanced fan section geometries. The numerical solutions demonstrated reasonable agreement with the experimental data and predicted boundary layer characteristics. It was apparent from the comparison to experiment that the Navier-Stokes solutions predicted the experimental data better than comparable Euler results. While grid resolution and tip clearance flow are important to predictive accuracy, boundary layer modeling has perhaps a stronger effect on predicting transonic fan performance. The accuracy of the analysis can also be effected by additional factors, including errors introduced by turbulence modeling and artificial dissipation.

REFERENCES

- [1] Celestina, M. L., Mulac, R. A., and Adamczyk, J. J., "A Numerical Simulation of the Inviscid Flow Through a Counterrotating Propeller", ASME Paper 86-GT-138, June 1986.
- [2] Adamczyk, J. J., Celestina, M. L., Beach, T. A., and Barnett, M., "Simulation of Three-Dimensional Viscous Flow Within a Multistage Turbine", ASME Paper 89-GT-152, June 1989.
- [3] Jameson, A., Schmidt, W., and Turkel, E., "Numerical solutions of the Euler Equations by Finite Volume Methods Using Runge-Kutta Time-Stepping Schemes", AIAA Paper AIAA-81-1259, June 1981.
- [4] Adamczyk, J. J., Mulac, R. A., and Celestina, M. L., "A Model for Closing the Inviscid Form of the Average-Passage Equation System", ASME Paper 86-GT-227, June 1986.
- [5] Hung, C. M., and Kordulla, W., "A Time-Split Finite Volume Algorithm for Three-Dimensional Flow-Field Simulation," AIAA Paper 83-1957, 1983.
- [6] Hollanders, H., Lerat, A., and Peyret, R., "Three-Dimensional Calculation of Transonic Viscous Flows by an Implicit Method," *AIAA Journal*, 23, pp. 1670-1678, 1985.
- [7] Jameson, A., and Baker, T. J., "Solution of the Euler Equations for Complex Configurations," AIAA Paper 83-1929, 1983.
- [8] Baldwin, B. S., and Lomax, H., "Thin-Layer Approximation and Algebraic Model for Separated Turbulent Flows", AIAA Paper 78-257, 1978.
- [9] Crook, A. J., and Delaney, R. A., "Investigation of Advanced Counterrotation Blade Configuration Concepts for High Speed Turboprop Systems: Task III - Advanced Fan Section Grid Generator, Final Report and Computer Program User's Manual", NASA CR 187129, NASA Contract NAS3-25270, 1991.

- [10] Crook, A. J., and Delaney, R. A., "Investigation of Advanced Counterrotation Blade Configuration Concepts for High Speed Turboprop Systems: Task IV - Advanced Fan Section Aerodynamic Analysis, Computer Program User's Manual", NASA CR 187127, NASA Contract NAS3-25270, 1992.
- [11] Sullivan, T. J., Luebering, G. W., and Gravitt, R. D., "Energy Efficient Engine Fan Test Hardware Detailed Design Report," NASA CR-165148, 1980.
- [12] Cline, S. J., Halter, P. H., Kutney, J. T., and Sullivan, T. J., "Energy Efficient Engine Fan and Quarter-Stage Component Performance Report," NASA CR-168070, 1982.

APPENDIX 'B'

ADPAC-APES DISTRIBUTION LIST

User's Manual Cr-187127

Final Report Cr-187128

Contract NAS3-25270

Task Order #4

GOVERNMENT AGENCIES:

NASA Headquarters

600 Independence Avenue, SW

Washington, DC 20546

ATTN: RJ/R. Whitehead

RP/N. Nijahawan

NASA Lewis Research Center

21000 Brookpark Road

Cleveland, OH 44135

ATTN: J.J. Adamczyk

C.L. Ball

L.J. Bober

D.R. Boldman

B. Clark

R.W. Claus

J.H. Dittmar

J.F. Groeneweg

C.E. Hughes

R.J. Jeracki

C.M. Kim

A.P. Kurkov

J. Lytle

C.J. Miller

D.P. Miller

R.D. Moore

D.V. Murthy

L.D. Nichols

C.W. Putt

D.R. Reddy

T.S. Reddy

R. Srivastava

G.L. Stefko

R.P. Woodward

J.A. Ziemianski

Report Control Office

Tech. Utilization Office

AFSC Liaison Office

M.S. 5-9 (2 copies)

M.S. 86-1

M.S. 77-6

M.S. 86-7

M.S. 77-6

M.S. 142-5

M.S. 77-6

M.S. 77-6 (4 copies)

M.S. 77-6

M.S. 77-6

M.S. 77-6

M.S. 23-3

M.S. ACC-1

M.S. 77-6 (15 copies)

M.S. 77-6

M.S. 77-6

M.S. 23-3

M.S. 142-5

M.S. 142-2 (2 copies)

M.S. 5-11

M.S. 23-3

M.S. 23-3

M.S. 23-3

M.S. 77-6

M.S. 86-1

M.S. 60-1 (4 copies)

M.S. 7-3

M.S. 501-3

NASA Ames Research Center
Moffett Field, CA 94035
ATTN: Library

M.S. 203-3

NASA Langley Research Center
Hampton, VA 23681-0001
ATTN: F. Farassat
S.L. Hodge
D. Stephens
Library

M.S. 460
M.S. 460
M.S. 462
M.S. 185

NASA Scientific & Technical
Information Facility
P.O. Box 8757
BWI Airport, MD 21240
ATTN: Accession Dept.

6 copies & FF427 form

Jason Assoc @ DARPA SUBTECH Center
David Taylor NSRDC
Bethesda, MD 20084
ATTN: C. Knight

Bldg. 17E, Room 120

Lockheed Engineering
and Sciences Company
144 Research Drive
Hampton, VA 23666
ATTN: M.H. Dunn

M.S. 904

Sverdrup Technology, Inc.
2001 Aerospace Parkway
Brookpark, OH 44142
ATTN: B. Berkowitz
R.M. Nallasamy
O. Yamamoto

SVR
SVR
SVR

INDUSTRY

AIRResearch Los Angeles Division
Allied-Signal Aerospace Company
P.O. Box 2960
Torrance, CA 90509-2960
ATTN: T. Booth

Dept. 93-209, T-42

Allison Gas Turbine Division, GMC Corp.
P.O. Box 420
Indianapolis, IN 46206-0420

ATTN: P.C. Tramm
R.F. Alverson
R.A. Delaney
D.W. Burns
J.F. Rathman
D.J. Helton
A.J. Crook
E.J. Hall
K.P. Nardini
J.L. Hansen
Library

M.S. T-11
M.S. T-14
M.S. T-14A
M.S. T-10B
M.S. T-02A
M.S. T-14A
M.S. T-14A
M.S. T-14A
M.S. T-14A
M.S. S-50
M.S. S-05

Boeing Commercial Airplane Company
(BCAC)
P.O. Box 3707
Seattle, WA 98124-2207

ATTN: B. Farquhar
W.H. Jou
R. Cuthbertson
G. Sengupta

M.S. 6M-98
M.S. 7H-96
M.S. 79-84
M.S. 7H-91

Douglas Aircraft Company Division
McDonnell Douglas Corporation
3855 Lakewood Boulevard
Long Beach, CA 90846

ATTN: M. Joshi
F. Lynch
G. Page
W. Siegele

M.S. 36-60
M.S. 36-60
M.S. 35-86
M.S. 202-15

General Dynamics Convair
P.O. Box 80844
San Diego, CA 92138

ATTN: B. Bergman
K. Taylor

M.Z. 36-1240
M.Z. 54-6890

General Electric Company
Aircraft Engine Group
1 Neumann Way
Evendale, OH 45215

ATTN: P. Gliebe
C. Lenhardt
M. Majjigi
M. Pearson
L. Smith
C. Whitfield

Mail Drop A-304
Mail Drop A-330
Mail Drop A-319
Mail Drop A-317
Mail Drop H-4
Mail Drop A-304

Hamilton Standard Division-UTC
Windsor Locks, CT 06096
ATTN: F.B. Metzger

M.S. 1A-3-6

Lockheed California Company
P.O. Box 551
Burbank, CA 91520
ATTN: Library

Pratt & Whitney Aircraft-UTC
Commercial Products Division
400 Main Street
East Hartford, CT 06108

ATTN: D.B. Hanson
D. Hopwood
D. Mathews
W. Lord
T. Wynosky

M.S. 165-11
M.S. 162-07 (3 copies)
M.S. 165-11
M.S. 169-23
M.S. 169-23

Rohr Industries, Inc.
P.O. Box 878
Chula Vista, CA 92012-0878
ATTN: Library

United Technologies Corporation
Research Center
Silver Lane
East Hartford, CT 06108

ATTN: M. Barnett
R. Davis
D. Dorney

M.S. 20
M.S. 20
M.S. 20

UNIVERSITIES

Georgia Institute of Technology
School of Aerospace Engineering
Atlanta, GA 30332-0800
ATTN: Dr. L.N. Sankar

Mississippi State University
Department of Aerospace Engineering
P.O. Box A
Mississippi State, MS 39762
ATTN: Dr. D. Whitfield
Dr. M. Janus